


A survey of high- z galaxies: SERRA simulations

A. Pallottini ^{1,★}, A. Ferrara ¹, S. Gallerani,¹ C. Behrens,² M. Kohandel ¹, S. Carniani ¹, L. Vallini ¹,
S. Salvadori ^{3,4}, V. Gelli ^{3,4}, L. Sommovigo,¹ V. D’Odorico ^{1,5,6}, F. Di Mascia¹ and E. Pizzati ^{1,7}

¹Scuola Normale Superiore, Piazza dei Cavalieri 7, I-56126 Pisa, Italy

²Institut für Astrophysik, Georg-August Universität Göttingen, Friedrich-Hund-Platz 1, D-37077 Göttingen, Germany

³Dipartimento di Fisica e Astronomia, Università degli Studi di Firenze, via G. Sansone 1, I-50019 Sesto Fiorentino, Italy

⁴INAF – Osservatorio Astrofisico di Arcetri, Largo E. Fermi 5, I-50125 Firenze, Italy

⁵INAF – Osservatorio Astronomico di Trieste, via G.B. Tiepolo 11, I-34143 Trieste, Italy

⁶Institute for Fundamental Physics of the Universe, Via Beirut 2, I-34151 Miramare, Trieste, Italy

⁷Leiden Observatory, Leiden University, Niels Bohrweg 2, NL-2333 CA Leiden, the Netherlands

Accepted 2022 May 2. Received 2022 April 29; in original form 2021 December 20

ABSTRACT

We introduce SERRA, a suite of zoom-in high-resolution ($1.2 \times 10^4 M_\odot$, $\simeq 25$ pc at $z = 7.7$) cosmological simulations including non-equilibrium chemistry and on-the-fly radiative transfer. The outputs are post-processed to derive galaxy ultraviolet (UV) + far-infrared (FIR) continuum and emission line properties. Results are compared with available multiwavelength data to constrain the physical properties [e.g. star formation rates (SFRs), stellar/gas/dust mass, metallicity] of high-redshift $6 \lesssim z \lesssim 15$ galaxies. This flagship paper focuses on the $z = 7.7$ sub-sample, including 202 galaxies with stellar mass $10^7 M_\odot \lesssim M_\star \lesssim 5 \times 10^{10} M_\odot$, and specific star formation rate ranging from $\text{sSFR} \sim 100 \text{ Gyr}^{-1}$ in young, low-mass galaxies to $\sim 10 \text{ Gyr}^{-1}$ for older, massive ones. At this redshift, SERRA galaxies are typically bursty, i.e. they are located above the Schmidt–Kennicutt relation by a factor $\kappa_s = 3.03_{-1.8}^{+4.9}$, consistent with recent findings for [O III] and [C II] emitters at high z . They also show relatively large InfraRed eXcess ($\text{IRX} = L_{\text{FIR}}/L_{\text{UV}}$) values as a result of their compact/clumpy morphology effectively blocking the stellar UV luminosity. Note that this conclusion might be affected by insufficient spatial resolution at the molecular cloud level. We confirm that early galaxies lie on the standard [C II]–SFR relation; their observed $L_{[\text{OIII}]} / L_{[\text{CII}]} \simeq 1\text{--}10$ ratios can be reproduced by a part of the SERRA galaxies without the need of a top-heavy initial mass function and/or anomalous C/O abundances. [O I] line intensities are similar to local ones, making ALMA high- z detections challenging but feasible (~ 6 h for an SFR of $50 M_\odot \text{ yr}^{-1}$).

Key words: methods: numerical – galaxies: evolution – galaxies: formation – galaxies: high-redshift – galaxies: ISM – infrared: general.

1 INTRODUCTION

Understanding the properties of galaxies in the epoch of the reionization (EoR; redshift $z \gtrsim 5.5$) is an urgent quest in modern physical cosmology. In the last decades, optical/near-infrared (IR) surveys have been used to identify galaxies, measure their star formation rates (SFRs), and follow their stellar mass build-up up to $z \sim 10$ (Dunlop 2013; Bouwens et al. 2015; Oesch et al. 2018). These data, in turn, inform cosmic reionization and metal enrichment models (see Dayal & Ferrara 2018; Maiolino & Mannucci 2019, for recent reviews).

Despite such magnificent progress, we know very little about a key component of the galactic ecosystem, i.e. the interstellar medium (ISM) of the early, ‘normal’, star-forming ($\text{SFR} \lesssim 100 M_\odot \text{ yr}^{-1}$) galaxy population. While *James Webb Space Telescope* (JWST) is about to give us access to the strong emission lines typically used to characterize the ISM properties at low z (e.g. Kewley & Dopita 2002; Curti et al. 2017), possibly augmented by machine learning

analysis techniques (Ucci et al. 2019), a complementary approach consists of using far-infrared (FIR) lines.

The Atacama Large Millimeter/submillimeter Array (ALMA) has enabled such exploration, in particular by exploiting the prominent (Stacey et al. 1991) [C II] 158 μm line. The earliest investigations of $z > 5$ targets reported a mix of upper limits (Kanekar et al. 2013; Ouchi et al. 2013; Ota et al. 2014; Schaerer et al. 2015) and detections (Capak et al. 2015; Maiolino et al. 2015; Watson et al. 2015; Willott et al. 2015). After such pioneering stage, [C II] is now routinely observed both in Lyman break galaxy (Carniani et al. 2017, 2018a; Smit et al. 2018; Hashimoto et al. 2019; Bakx et al. 2020), Lyman alpha emitters (Matthee et al. 2017; Carniani et al. 2018b; Harikane et al. 2018), and in gravitationally lensed, low-mass objects (Knudsen et al. 2016; Pentericci et al. 2016; Bradac et al. 2017). Today, FIR surveys containing hundreds of galaxies are being produced and analysed, both at just after ($4 \lesssim z \lesssim 6$; Le Fèvre et al. 2020, ALPINE) and well within ($6 \lesssim z \lesssim 8$; Bouwens et al. 2021, REBELS) the EoR.

Locally, it has been shown (e.g. Cormier et al. 2015) that [C II] traces essentially all ISM phases (cold/warm neutral, ionized) thus carrying very valuable and diverse information (see also Olsen et al. 2018). Initially, the comparison between EoR (Carniani et al. 2018a; Schaerer et al. 2020) and local (De Looze et al. 2014; Herrera-

* E-mail: andrea.pallottini@sns.it

Camus et al. 2015, 2018) data has mostly concentrated on the [C II]–SFR relation. Theoretical works followed the same path, by focusing on the interpretation of such relation and its connection with the burstiness of the star formation process (Ferrara et al. 2019; Pallottini et al. 2019; Vallini et al. 2020), parametrized via a deviation from the locally observed Schmidt–Kennicutt (Schmidt 1959; Kennicutt 1998) relation, and/or other parameters such as the ISM metallicity, density, and interstellar radiation field (ISRF; Vallini et al. 2013, 2015; Katz et al. 2017; Olsen et al. 2017; Pallottini et al. 2017a,b; Popping et al. 2019).

The investigation of early galaxies via [C II] line has nevertheless brought some genuine surprises, the most conspicuous of which is the detection of extended (up to 10 kpc) [C II] haloes around these sources. Such haloes have been first discovered in stacking experiments (Fujimoto et al. 2019; Ginolfi et al. 2020), and later confirmed individually in the most massive galaxies of the ALPINE sample (Fujimoto et al. 2020). A tantalizing explanation of this feature is that [C II] haloes are created by supernovae- (SNe) and/or active galactic nucleus-driven outflows (Pizzati et al. 2020) transporting carbon and other heavy elements in the circumgalactic medium (CGM). Notably, the [C II] line in these sources often shows extended wings produced by fast outflowing gas (Gallerani et al. 2018; Ginolfi et al. 2020).

We finally mention that [C II] observations are becoming deep enough to perform kinematic analysis (Jones et al. 2017; Smit et al. 2018; Schaerer et al. 2020), and interpreting via sophisticated models (Kohandel et al. 2019, 2020): Accurate rotation curves might allow us to set constraints on the role and amount of dark matter (DM) in these objects.

Given the multicomponent origin of the [C II] emission, complementary probes arising from a specific ISM phase are very valuable. Fortunately, the [O III] 88 μm , uniquely tracing dense ionized regions of the ISM, is observable and comes into rescue. Searches for such line (Inoue et al. 2016a; Carniani et al. 2017, 2020; Laporte et al. 2017a; Hashimoto et al. 2019; Tamura et al. 2019) have motivated interpretations of the observed morphological differences with respect to [C II] (Pallottini et al. 2019; Arata et al. 2020; Carniani et al. 2020; Harikane et al. 2020), and its use as a proxy for metallicity (Olsen et al. 2015; Inoue et al. 2016a; Vallini et al. 2017).

The molecular gas content and ISRF can instead be probed via CO roto-vibrational lines (Vallini et al. 2018, 2019). High- J CO lines can also be used to explore the possible presence of X-ray sources and shocks in these galaxies (Gallerani et al. 2014; Vallini et al. 2019). However, CO emission is faint and it has only been detected in a few EoR objects (D’Odorico et al. 2018; Pavesi et al. 2019), sometimes in a serendipitous manner (Feruglio et al. 2018).

As for the dust FIR continuum emission, it entails considerable uncertainties as the dust mass and temperature are degenerate and often hard to determine in high- z sources (e.g. Faisst et al. 2020; Fudamoto et al. 2020). Available ALMA observations sample the FIR regime with very few data points (sometimes even a single one) making it hard to break the degeneracy. Some theoretical works predict that dust should be warmer at high z (Behrens et al. 2018; Liang et al. 2019; Sommovigo et al. 2020, 2021; Di Mascia et al. 2021); others claim that dust production is more efficient early on (Mancini et al. 2015; Popping, Somerville & Galametz 2017). To make progress, it would be necessary to probe wavelengths bluewards of the blackbody peak by means of mid-infrared (MIR) observations. Given the cancellation of the *Space Infrared Telescope for Cosmology and Astrophysics* (Spinoglio et al. 2017; Egami et al. 2018) and *Origins Space Telescope* (Cooray et al. 2020) missions, novel strategies must be urgently devised.

To conclude, the study of the ISM of EoR galaxies is in its infancy. The investigation of the ISM is crucial to answering key open physical questions concerning these sources: What is their star formation efficiency? How various (mechanical, radiative, chemical) feedback processes affect the thermal, dynamical, and turbulent state of the ISM? What is the amount of dust, metals, and molecular gas in these systems? These questions could be finally attacked by combining ALMA and *JWST* data.

From a theoretical point of view, progressively more refined and physics-rich numerical simulations represent an indispensable guideline and tool. Since we would like to resolve the ISM down to the molecular cloud (MC) level, suitable simulations should reach a (baryonic) mass resolution $\simeq 10^4 M_\odot$, and be able to probe $\simeq 10$ pc scales. While not as critical as for simulations that aim at studying the reionization process (e.g. CROC, Gnedin 2014; SPHINX, Rosdahl et al. 2018; CODA II, Ocvirk et al. 2020), the ISRF is an important physical ingredient for early galaxy evolution (Katz et al. 2017; Trebitsch et al. 2017; Pallottini et al. 2019). Thus, radiative transfer should be consistently implemented.

As smaller scales are resolved, a better prescription of unresolved (sub-grid) processes must be included with respect to coarser large-scale cosmological simulations (mass resolution $\simeq 10^6 M_\odot$ and $\simeq 0.2$ – 1 kpc scales, e.g. EAGLE, Schaller et al. 2015, BLUETIDES, Feng et al. 2016, ILLUSTRIS-TNG, Pillepich et al. 2018, and THESAN, Kannan et al. 2022), in order to properly account for the turbulent structure of the ISM, its chemical state, and stellar feedback (Agertz et al. 2013; Hopkins et al. 2014; Agertz & Kravtsov 2015; Pallottini et al. 2017a,b; Lupi 2019). This makes it demanding to simulate a large galaxy sample in an unbiased cosmological volume with high resolution and a variety of sub-grid models.¹

A more efficient option is to perform multiple zoom-in simulations, as done e.g. in Ma et al. (2018, see FIRE-2 Hopkins et al. 2018 for the models), Ceverino, Glover & Klessen (2017, FIRSTLIGHT), and Lovell et al. (2021, FLARES). With some efforts (see in particular Lovell et al. 2021), multiple zoom-in simulations can be used to construct a composite sample that is representative of the parent cosmological volume used for the zoom-in.

In this paper, we present SERRA,² a suite of multiple zoom-in cosmological simulations targeting $M_\star \sim 10^8$ – $10^{10} M_\odot$ galaxies at $z = 6$. Each simulation follows the evolution of 10–30 galaxies in a cosmological environment by employing a radiation-hydrodynamic code that is coupled to a non-equilibrium chemical network. In this work, we analyse the results from 10 simulations focusing at $z = 7.7$, for a total of 202 galaxies. Here, we do not aim at building a fully unbiased cosmological galaxy sample. Rather, we intend to mimic a survey targeting galaxies that are luminous enough to be detected and characterized with current (*Hubble Space Telescope* and ALMA) and upcoming instruments (*JWST*). Paralleling current [C II] observational campaigns with ALMA (Le Fèvre et al. 2020; Bouwens et al. 2021), we can then reconstruct at a later stage the statistical properties (Béthermin et al. 2020) of our sample, at the same time spotting interesting or peculiar objects (Fudamoto et al. 2021; Loiacono et al. 2021).

Most of the assumptions and techniques adopted in SERRA have already been developed in previous works. In Pallottini et al.

¹ See e.g. the ‘normal’ volume of the RENAISSANCE from O’Shea et al. (2015), where the simulation focuses on a $\simeq (6 \text{ Mpc}^3)$ region and it is stopped around $z \simeq 12$.

² SERRA means greenhouse in Italian. You might notice that galaxies are named after flowers (and some also look alike).

(2017a), we focused on the modelling of stellar feedback; Pallottini et al. (2017b) showed the impact of non-equilibrium chemistry; in Pallottini et al. (2019), we analysed the impact of radiation-hydrodynamical effects. Advanced line and continuum emission models, a foundational feature of SERRA, are based on Vallini et al. (2015, 2019) and Behrens et al. (2018), respectively. The simulation results are post-processed to produce synthetic data cubes (Kohandel et al. 2020), which can be directly and fairly compared with observations (Behrens et al. 2018; Gelli et al. 2021; Zanella et al. 2021).

The paper plan is as follows. In Section 2, we summarize the main features and assumptions of the SERRA simulations. In Section 3, we present our results. We analyse the stellar mass build-up and time evolution of the simulated galaxies (Sections 3.1 and 3.2). Focusing on the $z = 7.7$ sample, we study the halo mass-to-stellar mass relation (Sections 3.3 and 3.3.1), the Schmidt–Kennicutt relation (Section 3.4), and the size–mass relation (Section 3.5). Then in Section 3.6, we explore the main FIR and ultraviolet (UV) properties, treating both continuum (Sections 3.6.1 and 3.6.2) and line (Section 3.6.3) emission. Section 4 provides a summary.

2 NUMERICAL SIMULATIONS

In SERRA, the dynamical evolution of DM, gas, and stars is simulated with a customized version of the adaptive mesh refinement (AMR) code RAMSES³ (Teyssier 2002). RAMSES follows the gas evolution with a second-order Godunov scheme; DM and stars are treated with a multigrid particle-mesh solver (Guillet & Teyssier 2011). Radiative transfer is solved on-the-fly using RAMSES-RT (Rosdahl et al. 2013), which implements photon advection using a momentum-based framework with M1 closure for the Eddington tensor (Aubert & Teyssier 2008). While photon transport is handled by RAMSES-RT, the system of equations regulating gas–photon interactions (including the gas thermal evolution) is generated via KROME⁴ (Grassi et al. 2014) adopting a non-equilibrium chemical network (Bovino et al. 2016; Pallottini et al. 2017b). The coupling between KROME and RAMSES-RT is done by sub-cycling the absorption step in order to assure convergence (see also Decataldo et al. 2019; Pallottini et al. 2019).

Critical to a fair comparison with observations is the production of line and continuum emission. This is done in post-processing by adopting multiple models. Emission lines are calculated by interpolating grids of models obtained from the photoionization code CLOUDY c17⁵ (Ferland et al. 2017), by extending Vallini et al. (2017) models as described in Pallottini et al. (2019). Attenuated UV and continuum FIR emission is computed via the Monte Carlo code SKIRT V8⁶ (Baes & Camps 2015; Camps & Baes 2015), using the modelling from Behrens et al. (2018).

In the following, we summarize the main features of the numerical set-up (Section 2.1), radiation hydrodynamics (Section 2.2), stellar modelling (Section 2.3), and galaxy identification and emission properties (Section 2.4).

2.1 Set-up

We generate cosmological initial conditions (ICs) assuming parameters compatible with *Planck* results.⁷ ICs are computed with

MUSIC (Hahn & Abel 2011) at $z = 100$ for a cosmological volume of $(20 \text{ Mpc } h^{-1})^3$, which will contain $\simeq 7$ haloes with masses $M_h \geq 10^{11} M_\odot$ at $z = 6$ (Murray, Power & Robotham 2013, adopting a Sheth & Tormen 1999 halo mass function). The base grid has eight levels, equivalent to a gas (DM) mass of $6 \times 10^6 M_\odot$ ($3.6 \times 10^7 M_\odot$). We run a total of 11 simulations, and for each simulation, we prepare distinct ICs; we then evolve the volume down to $z = 6$. We use HOP (Eisenstein & Hu 1998) to extract halo catalogues and select a target among the most massive haloes in the simulated cosmological volume. These have $M_h \simeq (1-5) \times 10^{11} M_\odot$ (corresponding to $\simeq 3.2-4.1\sigma$ fluctuations), and thus they are resolved with about $(2-16) \times 10^3$ particles in the coarse runs.

Using HOP, we select the minimum ellipsoid enveloping about six times the halo virial radius (r_{vir}), and trace it back to $z = 100$. Haloes with $M_h = (1-5) \times 10^{11} M_\odot$ have virial radii of $\simeq 20-35$ kpc. A comoving *trace back* radius of about $1-2 \text{ Mpc } h^{-1}$ is typically obtained. We select such Lagrangian volume at $z = 100$ and using MUSIC we produce multimass ICs, i.e. we progressively add concentric layers of increasing mass resolution around the target. We reach 11 levels in the zoom-in region, i.e. a gas (DM) mass of $1.2 \times 10^4 M_\odot$ ($7.2 \times 10^4 M_\odot$). Such Lagrangian volume is then evolved at $z = 6$ and the main halo is resolved with about $(1-7) \times 10^6$ DM particles in these zoom-in runs.

In the zoom-in region, we set 6 additional AMR levels (thus 17 in total), which are enabled via a Lagrangian-like criterion. This allows us to reach spatial scales of $\simeq 30$ pc ($\simeq 25$ pc) at $z = 6$ ($z = 7.7$) in the densest regions, i.e. the most refined cells have mass and size typical of Galactic MCs ($10-50$ pc, $10^4-10^6 M_\odot$; Federrath & Klessen 2013).

Adopting a trace back radius of $\simeq 6r_{\text{vir}}$ typically ensures negligible contamination for the central halo (Onorbe et al. 2014). However, here we are also interested in other galaxies in the proximity of the target. For this reason, we perform the target selection and trace back procedure two times (cf. Fiacconi, Feldmann & Mayer 2015). This limits the contamination levels to $\simeq 0.1$ per cent ($\simeq 2$ per cent) for the target (surrounding) haloes in the zoom-in region; from the analysis, we exclude galaxies with a contamination of ≥ 4.3 per cent within $2r_{\text{vir}}$. With this threshold, the resulting sample has an average⁸ contamination level of $0.0^{+0.7}_{-0.0}$ per cent ($1.1^{+0.6}_{-0.4}$ per cent) when considering $1r_{\text{vir}}$ ($2r_{\text{vir}}$). Further, the apparently higher contamination of some of the galaxies in the simulations (Onorbe et al. 2014) is mostly due to the adopted definition, i.e. we are considering all DM particles within $2r_{\text{vir}}$ (of the host DM) from the centre of a galaxy, while $1r_{\text{vir}}$ is adopted in most works.

2.2 Radiation hydrodynamics

2.2.1 Gas and dust composition

The chemical network in the simulations includes H, H⁺, H⁻, He, He⁺, He⁺⁺, H₂, H₂⁺, and electrons. Each of these species is tracked individually, and evolves according to the chemical processes described in Section 2.2.3. Metallicity (Z) is tracked as the sum of heavy elements, and we assume solar abundance ratios of the different metal species (Asplund et al. 2009). Numerically, metallicity is treated as a passively advected scalar, and stars act as a source of metals and reprocessed material (Section 2.3). Dust

$H_0 = 67.8 \text{ km s}^{-1} \text{ Mpc}^{-1}$, spectral index $n = 0.967$, and $\sigma_8 = 0.826$ (Planck Collaboration et al. 2014).

⁸When giving averages, we are quoting the median value of the distribution with errors based on the values of 25 per cent and 75 per cent of the data set.

³<https://bitbucket.org/rteyssie/ramses>

⁴<https://bitbucket.org/tgrassi/krome>

⁵<https://www.nublado.org>

⁶<https://www.skirt.ugent.be>

⁷ Λ CDM model with vacuum, matter, and baryon densities in units of the critical density $\Omega_\Lambda = 0.692$, $\Omega_m = 0.308$, $\Omega_b = 0.0481$, Hubble constant

evolution is not explicitly tracked during simulation. We make the assumption that the dust-to-gas mass ratio scales with metallicity, i.e. $\mathcal{D} = \mathcal{D}_\odot(Z/Z_\odot)$, where $f_d = \mathcal{D}_\odot/Z_\odot = 0.3$ for the Milky Way (MW; e.g. Hirashita & Ferrara 2002). For chemical reactions involving dust and radiation absorption, we assume an MW-like grain size distribution (Weingartner & Draine 2001).

Individual ICs for the various chemical species are computed accounting for the chemistry in a primordial Universe (Galli & Palla 1998). We adopt an initial metallicity floor $Z_{\text{floor}} = 10^{-3} Z_\odot$ since at $z \gtrsim 40$ our resolution does not allow us to track the formation of first stars (see Wise et al. 2012; O’Shea et al. (2015); Smith et al. 2018). Such floor only marginally affects the gas cooling time (see also Section 2.2.3), and it is compatible with the metallicity of the intergalactic medium (IGM) in cosmological simulations (e.g. Pallottini et al. 2014; Maio & Tescari 2015; Jaacks et al. 2018). Such set-up is fully described in Pallottini et al. (2017b).

2.2.2 Photons

In RAMSES-RT, photons are treated as a fluid sharing the same AMR structure of the gas. Photons are divided into energy bins, whose density and velocity fields are tracked separately.

As done in Pallottini et al. (2019), in SERRA, we follow five photon bins in the 6.0–24.59 eV range.⁹ The first two energy bins cover the Habing (1968) band¹⁰ 6.0–13.6 eV, which regulates the temperature of the ISM and photodissociation regions (PDRs); of the two, the higher energy bin is specific for the Lyman–Werner radiation (11.2–13.6 eV), which photodissociates H₂ via the two-step Solomon process (Stecher & Williams 1967). The last three energy bins cover the H-ionizing photons up to the first ionization level of He (13.6–24.59 eV). For H-ionizing photons, the energy width is chosen such that the bins have the same number of photons when the spectral energy distribution (SED) is averaged over a selected fiducial stellar population – i.e. age 10 Myr and $Z_* = Z_\odot$ assuming Bruzual & Charlot (2003) photoionization models – since these stars dominate the spectrum of a galaxy with an exponentially rising SFR (e.g. Pallottini et al. 2017b).

Gas and dust represent sinks for the radiation (Section 2.2.3), while stars act as sources (Section 2.3.2). We neglect the cosmic UV background (UVB) contribution, since the typical ISM densities are sufficiently large to ensure an efficient self-shielding (Gnedin 2010). In the EoR, the UVB produces a statistically negligible hydrogen ionization for gas with density $n \gtrsim 10^{-2} \text{ cm}^{-3}$, i.e. close to those found in the outskirts of early galaxies (Rahmati et al. 2013; Chardin, Kulkarni & Haehnelt 2018). We do not account for recombination radiation, i.e. we assume that recombination photons are absorbed ‘on the spot’ (Rosdahl et al. 2013).

Both RAMSES and RAMSES-RT have explicit schemes; thus, the time-step of a fluid with velocity v is limited by the Courant condition (Courant, Friedrichs & Lewy 1928), i.e. $\Delta t \sim \Delta l/v$. As radiation and gas evolution are coupled, the maximum speed is selected, i.e. the speed of light. To limit the computational load, we consider the *reduced speed of light* approximation to propagate wavefronts (Gnedin & Abel 2001).

The reduced speed of light approach might produce artefacts in regions where the dissociation/ionization front propagation is faster than the reduced speed of light, c_{red} , used in the simulation. For instance, in reionization studies, $c_{\text{red}} \sim 10^{-1}c$ allows one to resolve

the cosmological I-front propagation, yielding little variations on global reionization histories (Gnedin 2016, see also Deparis et al. 2019, where the effect is explored in the $10^{-2} \leq c_{\text{red}}/c \leq 1$ range). For PDRs, the speed of the wavefront can be estimated as

$$v_{\text{PDR}} = \frac{G}{n(h\nu)_{\text{FUV}}} \sim 5 \times 10^{-3} \frac{G}{10^3 G_0} \frac{5 \times 10^2 \text{ cm}^{-3}}{n} c, \quad (1)$$

where we have used the typical values expected for high- z galaxies with the photon-to-baryon ratio particularly high, e.g. as in the case of a $\sim 10^5 M_\odot$ newly born star cluster in a typical Giant Molecular Cloud (GMC).

In Pallottini et al. (2019), we adopted a conservative value of $c_{\text{red}} = 10^{-2}c$; however, there we also noted that the PDR size is set by the dust optical depth $\tau_d = 1$. This yields

$$l_{\text{PDR}} = \frac{\mathcal{D}}{\mathcal{D}_\odot} \frac{10^{21} \text{ cm}^{-2}}{n} \sim 0.6 \frac{\mathcal{D}}{\mathcal{D}_\odot} \frac{5 \times 10^2 \text{ cm}^{-3}}{n} \text{ pc}, \quad (2)$$

implying that PDRs are typically unresolved in our simulations. The PDR is established in a time

$$t_{\text{PDR}} = \frac{l_{\text{PDR}}}{v_{\text{PDR}}} \simeq 390 \frac{\mathcal{D}}{\mathcal{D}_\odot} \frac{10^3 G_0}{G} \text{ yr} \quad (3)$$

then the propagation of the front slows down below v_{PDR} . Depending on the dust amount and the ISRF value, reducing the speed of light to a value lower than $c_{\text{red}} = 5 \times 10^{-3}c$ is expected to affect only the evolution in a fraction of Myr, as we also show in Decataldo et al. (2019). A different situation is when radiation breaks out of the birth clouds and impacts the rest of the galaxy; after $\simeq 20$ Myr, a $\sim 10^5 M_\odot$ cluster would produce in its surrounding an ISRF of $G \sim 10 G_0$; assuming that the SN feedback has cleared out the gas, we expect gas densities of the order of $n \sim 10^{-2} \text{ cm}^{-3}$, thus from equation (1) it follows that $v_{\text{PDR}} = c$, i.e. the reduced speed of light approximation breaks down (see Gnedin 2016, for a similar issue); however, the PDR is already established in $\lesssim 1$ Myr (equation 3); thus, the situation is expected to be relatively rare in our simulations.¹¹ Moreover, the breakdown of the approximation is not expected to affect satellites, as the dominant contribution to the ISRF is generated *in situ*, because of geometrical dilution (Gelli et al., in preparation).

Further, in Lupi et al. (2020), we adopted the same ICs used in Pallottini et al. (2019), but with a different numerical code, and a lower speed of light, i.e. $c_{\text{red}} = 10^{-3}c$. We noted no large differences in properties of the target galaxy in the two zoom-in (e.g. SFR, M_* , average ISM density, ISRF value, etc.). This is consistent with what found in Hopkins et al. (2020), where variations of $10^{-3} \lesssim c_{\text{red}} \lesssim 10^2$ are shown to affect the ISM properties through a slight variation of the radiation pressure efficiency.

For this reason, we adopt $c_{\text{red}} = 10^{-3}c$ in the present, which – with respect to Pallottini et al. (2019) – also allow us to zoom in relatively larger Lagrangian volumes and higher sigma fluctuations by spending roughly the same computational time.

2.2.3 Chemical processes

Our KROME-powered non-equilibrium network follows a total of 48 reactions,¹² including photochemistry, dust processes, and cosmic

⁹For He and He⁺, we assume collisional ionization only.

¹⁰In this paper, the Habing flux G is indicated in units of $G_0 = 1.6 \times 10^{-3} \text{ erg cm}^{-2} \text{ s}^{-1}$, the MW value.

¹¹A similar reasoning applies also to H-ionizing photons, since they are scarcely emitted after the stars producing them turn into SNe.

¹²The reactions, their rates, and corresponding references are listed in appendix B of Bovino et al. (2016): We use reactions from 1 to 31 and 53, 54, from 58 to 61, and from P1 to P9; the rates are reported in tables B.1, B.2, and 2 of Bovino et al. (2016), respectively.

ray-induced reactions (Pallottini et al. 2017b, see Bovino et al. 2016 for the original implementation).

Molecular hydrogen is particularly important in SERRA, since it determines the star formation process (Section 2.3.1). Formation of H_2 is possible both in gas phase and on dust grain surfaces. The formation rate of H_2 on dust grains is approximated following Jura (1975):

$$R_{H_2\text{-dust}} = 3 \times 10^{-17} n n_H \frac{D}{D_\odot} \text{ cm}^{-3} \text{ s}^{-1}, \quad (4)$$

where n and n_H are the total and hydrogen gas densities, respectively. Note that the dust channel is dominant with respect to the gas-phase formation channel for $D \gtrsim 10^{-2} D_\odot$, i.e. for most of the lifetime of a typical EoR galaxy (Pallottini et al. 2017b).

Cosmic rays are not explicitly tracked in the simulation (cf. Dubois & Commerçon 2016; Pfrommer et al. 2017). Similarly to what is done in Pallottini et al. (2017b, 2019), we assume a cosmic ray hydrogen ionization – and associated Coulomb heating – rate proportional to the global SFR (Valle et al. 2002) and normalized to the MW value (Webber 1998, see Ivlev et al. 2015; Padovani et al. 2018 for the spectral dependence), i.e. $\zeta_{\text{cr}} = 3 \times 10^{-17} (\text{SFR}/M_\odot \text{ yr}^{-1}) \text{ s}^{-1}$. Note that the global SFR is computed by averaging over the stellar mass formed in the whole simulation in the last 20 Myr, and it is typically dominated by the target galaxy in the zoom-in region (see also Pallottini et al. 2017a). Note that this likely overestimates the ionization and heating from cosmic rays; while it is possible to track the cosmic ray field consistently (Farcy et al. 2022), we leave such modification for a future work.

Using on-the-fly radiative transfer, absorption is done on a cell-by-cell basis. The process depends on the abundance of each single species, dust amount, and the selected MW grain size distribution.¹³ Cross-sections for gas processes are directly taken from the reaction rates of the network. For photoreactions, in each radiation bin, the relative cross-section is pre-computed and averaged on the SED of the fiducial stellar population. The self-shielding of H_2 from photodissociation is accounted given the H_2 column density, temperature, and turbulence (Richings, Schaye & Oppenheimer 2014).

KROME solves the chemical and thermal evolution by adopting DLSODES (Hindmarsh 2019), an implicit solver that takes advantage of the sparsity of Jacobian matrix associated with an astrophysical chemical network. As noted in Pallottini et al. (2019), in its current version, KROME evolves chemical species by assuming that the radiation field is constant in a time-step; to account for absorption associated with chemical processes, we sub-cycle the absorption step in order to assure convergence (Decataldo et al. 2019, in particular see the benchmarks in their appendix).

2.2.4 Gas thermodynamics

We model both the evolution of thermal and turbulent (or non-thermal) energy content of the gas.

Thermal energy can change due to radiative cooling and heating, which are computed using KROME and accounting for the local ISRF. Extra thermal energy inputs are due to stellar feedback (e.g.

SNe and winds, see Section 2.3.2). Since metal species are not followed individually, we use the equilibrium metal line cooling function calculated via CLOUDY (Ferland et al. 2013) with a Haardt & Madau (2012) UVB.¹⁴ Following cooling from individual metal species can modify the thermodynamics of the low-density ISM (Gnedin & Hollon 2012; Capelo et al. 2018), since the cooling function typically changes by a factor of $\lesssim 2$ (Bovino et al. 2016). Such effect might be important to correctly compute emission line strengths, particularly for some lines (Lupi et al. 2020). To overcome this problem and to reach a better accuracy, in SERRA we perform this computation in post-processing (Sections 2.4.2 and 2.4.3). Dust cooling is not explicitly included since it gives a minor contribution to the gas temperature for $n < 10^4 \text{ cm}^{-3}$ (Bovino et al. 2016, see their fig. 3). Note that the cosmic microwave background effectively sets a temperature floor for the gas. Its inclusion is fully described in Pallottini et al. (2017b).

The non-thermal energy density e_{nth} of the gas is treated as a passively advected variable (Agertz & Kravtsov 2015), which is sourced by stellar feedback (e.g. SNe, winds, and radiation pressure, see Section 2.3.2). Once turbulence is injected in the gas, it can dissipate at a rate (Teyssier et al. 2013, see equation 2)

$$\dot{e}_{\text{nth}} = -\frac{e_{\text{nth}}}{t_{\text{diss}}}, \quad (5)$$

where t_{diss} is the dissipation time-scale. This can be written as the eddy turnover scale (Mac Low 1999)

$$t_{\text{diss}} = 9.785 \left(\frac{\Delta l}{100 \text{ pc}} \right) \left(\frac{\sigma_t}{10 \text{ km s}^{-1}} \right)^{-1} \text{ Myr}, \quad (6)$$

where $\sigma_t = \sqrt{e_{\text{nth}}}$ is the turbulent velocity dispersion. More refined turbulence models are available (Scannapieco & Brügggen 2010; Iapichino, Federrath & Klessen 2017; Engels, Schmidt & Niemeyer 2019), and have been successfully used in zoom-in simulation (Semenov, Kravtsov & Gnedin 2016, 2018). However, they have not been adopted in the present since the resulting SFR efficiencies are comparable (Pallottini et al. 2017a).

2.3 Stars

Stellar particles in the simulation have a minimum mass of $m_\star^{\text{min}} = 1.2 \times 10^4 M_\odot$, the gas mass resolution in the zoom-in region. Thus, a single star particle in our simulations should be rather seen as a proxy for a ‘stellar cluster’. We assume a 0.1–100 M_\odot Kroupa (2001) initial mass function (IMF). We keep track of the metallicity and age of each stellar particle. This information is used to compute chemical, radiative, and mechanical feedback via STARBURST99 (Leitherer et al. 1999), by adopting evolutionary tracks of stellar population from PADOVA (Bertelli et al. 1994) library, that covers the $0.02 \leq Z_\star/Z_\odot \leq 1$ metallicity range.

2.3.1 Star formation

Stars form according to a Schmidt–Kennicutt relation (Schmidt 1959; Kennicutt 1998) that depends on the molecular hydrogen density (n_{H_2}):

$$\rho_{\text{SFR}} = \zeta_{\text{SFR}} \frac{\mu m_p n_{H_2}}{t_{\text{ff}}}, \quad (7)$$

¹⁴This is inconsistent; for a discussion, see Pallottini et al. (2017b) and Emerick, Bryan & Mac Low (2019, in particular appendix D), the latter showing that the largest difference can be found for gas with $0.1 \lesssim n/\text{cm}^{-3} \lesssim 1$.

¹³A different assumption on the dust distribution can give relevant effects on the observed SED (Behrens et al. 2018); however, it typically gives only minor differences for the chemical network. For instance, adopting a Small Magellanic Cloud or MW composition has average differences of $\simeq 1$ per cent, which goes up to $\simeq 30$ per cent for energy bins that contribute neither to H_2 dissociation nor to H ionization (Pallottini et al. 2019).

where ρ_{SFR} is the local star formation rate density, ζ_{SFR} the efficiency, m_{p} the proton mass, μ the mean molecular weight, and t_{ff} the local free-fall time. The efficiency is set to $\zeta_{\text{SFR}} = 10$ per cent, i.e. adopting the average value observed for MCs (Murray 2011, see also Agertz et al. 2013).

Equation (7) is solved stochastically at each time-step Δt in each cell (size Δl) (Rasera & Teyssier 2006; Dubois & Teyssier 2008), by forming a new star particle with mass $m_{\star} = m_{\star}^{\text{min}} N_{\star}$, with N_{\star} an integer drawn from a Poisson distribution characterized by mean

$$\langle N_{\star} \rangle = \zeta_{\text{SFR}} \frac{\mu m_{\text{p}} n_{\text{H}_2} \Delta l^3 \Delta t}{m_{\star}^{\text{min}} t_{\text{ff}}}. \quad (8)$$

For numerical stability, no more than half of the cell mass is allowed to turn into stars. The stellar metallicity, Z_{\star} , is set equal to the gas metallicity, Z , of the spawning gas cell.

2.3.2 Stellar feedback

Stellar energy inputs, chemical yields, and photon production depend both on metallicity Z_{\star} and age t_{\star} of the stellar cluster, according to the PADOVA tracks. Stellar feedback includes SNE, winds from massive stars, and radiation pressure (see also Agertz et al. 2013).

Depending on the kind of feedback, stellar energy input can be both thermal and kinetic, and we account for the dissipation of energy in MCs for SN blastwaves (Ostriker & McKee 1988) and OB/AGB stellar winds (Weaver et al. 1977). The relative fraction of thermal and kinetic energy depends on the SN blast stage: energy conserving Sedov–Taylor stage (about 70 per cent thermal, 30 per cent kinetic), shell formation stage, and pressure-driven snowplough (about 15 per cent thermal and 35 per cent kinetic). This is detailed in section 2.4 and appendix A of Pallottini et al. (2017a).

Note that radiation pressure is implemented by adding a source term to the turbulent (non-thermal) energy, as detailed in Pallottini et al. (2017a). Thus, to avoid double counting of such feedback, we turn off the standard radiation pressure prescription of RAMSES-RT (Rosdahl & Teyssier 2015).

2.4 Post-processing

After each individual zoom-in simulation is completed, we identify galaxies and compute their emission properties. Each simulation outputs multiple snapshots equispaced in redshift ($\Delta z \simeq 0.5$) for $15 \leq z \leq 9$ and equispaced in time ($\Delta t \simeq 10$ Myr) for $9 \leq z \leq 6$; this set-up gives a total of about 70 snapshots per simulation. In each snapshot, apart from the central target, there are about 10–30 galaxies in the zoom-in region, depending on environment and redshift.

2.4.1 Identification

To identify DM haloes and galaxies, we use ROCKSTAR-GALAXIES¹⁵ (Behroozi, Wechsler & Wu 2013a), a clustering algorithm that performs a phase-space identification for multimass simulations. It uses a friend-of-friend algorithm that adopts a metric accounting for both spatial and velocity separations. We treat separately DM and stellar particles, and allow ROCKSTAR-GALAXIES to identify groups with a minimum number of 100 (20) DM (stars) particles. While

¹⁵<https://bitbucket.org/pbehoorzi/rockstar-galaxies>

ROCKSTAR-GALAXIES provides the linking relations between sub-halo (satellites) and halo (main galaxy), in this paper, we treat each galaxy as an individual object. We note that using a typical parametrization for the phase-space distances is too coarse to allow a complete and robust identification of dwarf satellites of high- z galaxies (cf. Gelli et al. 2020).

To identify progenitors/descendants through cosmic time, we use an algorithm similar to MERGERTREE (Knebe et al. 2013). First, we produce all the galaxy/DM halo catalogues of each snapshot. For each consecutive couple of snapshots, we cross-match the galaxies/DM haloes identified in the two catalogues.

Given two snapshots at redshift $z_1 < z_2$, the halo A at z_1 is flagged as a progenitor of the halo B at z_2 if their intersection has $N_{A \cap B} > 100$ DM (20 stellar) particles. The main progenitor of B is the halo A that maximizes the merit function $\mathcal{M}_1 = N_{A \cap B}^2 / N_A N_B$ (Srisawat et al. 2013). Using the progenitor list for each couple of consecutive snapshots, we can build the full progenitor/descendant graph for each galaxy and halo. If two galaxies keep exchanging mass (e.g. during a merger spanning multiple snapshots), we supplement our progenitor search by cross-matching the progenitor catalogue with the descendant catalogue. The latter is obtained by looking for haloes in snapshot z_2 that are descendant haloes in snapshot z_1 , with the same procedure outlined above. Considering only particle IDs in the progenitor/descendant identification is prone to a potential misidentification of progenitors/descendants (Srisawat et al. 2013) and can be avoided by adding dynamical information (see e.g. CONSISTENT-TREES from Behroozi et al. 2013b). However, (i) the fine time sampling of our snapshots ameliorates the problem and (ii) we scarcely use such information in this study; thus, we will consider such treatment in future work.

Finally, we label a galaxy by the name of the simulation, number of the snapshot, and stellar halo ID, and we often indicate it with a specific name.¹⁶

2.4.2 Line emission

Line emission is calculated on a cell-by-cell basis by using CLOUDY models. We use grids of CLOUDY models for density, metallicity, and radiation field intensity, as a function of the column density, which is used as a stopping criterion for the calculation. We account for the turbulent and clumpy structure of the ISM, by parametrizing the underlying distribution as a function of the gas Mach number (Vallini et al. 2017, 2018), expressing the thermal-to-turbulent energy ratio. We have two grids of CLOUDY models, in which the impinging SED includes – does not include – ionizing radiation ($h\nu > 13.6$ eV). We consider radiation to be ionizing in those cells that (i) contain young ($t_{\star} \leq 10$ Myr) stars or (ii) have an ionization parameter larger than $\geq 10^{-3}$.

Every grid is composed of 17 density bins ($10^{-2} \leq n/\text{cm}^{-3} \leq 10^{6.5}$), 8 metallicity bins ($10^{-3} \leq Z/Z_{\odot} \leq 10^{0.5}$), and 12 ISRF intensity bins ($10^{-1} \leq G/G_0 \leq 10^{4.5}$), for a total of 1632 distinct models per grid. For the SED of the impinging radiation field on the slab of gas of interest in CLOUDY, we use our fiducial SED with stellar age of 10 Myr and solar metallicity, i.e. the stellar population is the primary contributor to the ISRF in our simulated galaxies. Note that in the post-processing via CLOUDY, the spectrum is not

¹⁶When a specific name is chosen for a galaxy, it is propagated through the main progenitor and descendant branch of its graph. For instance, ‘Freesia’ is the most massive galaxy in *serra00*: It has been identified at $z \simeq 8$ and its main characteristics have been described in Pallottini et al. (2019).

limited to 24.59 eV. The full set-up is described in Pallottini et al. (2019), while in Lupi et al. (2020), a detailed analysis of different emission line models is reported (see Olsen et al. 2018, for additional discussion).

Line emission products can be spatially resolved maps or hyperspectral data cubes, i.e. line spectra in a position–position–line of sight velocity space (Kohandel et al. 2020). Given a field of view (FOV) and a line of sight, for optically thin lines (e.g. FIR lines such as [C II] 158 μm), we can directly sum the contribution of all the gas cells in the FOV. For optically thick lines (e.g. C III] 1909 \AA), we should consider the radiative transfer through dust (see Behrens et al. 2019, for the additional efforts needed for Ly α). Unattenuated (de-reddened) emission lines can be readily calculated and approximate treatments for the attenuation can give reliable estimates (Gelli et al. 2021); however, we defer more refined implementations to future work.

2.4.3 Continuum emission

Continuum emission is generated by using SKIRT, a Monte Carlo-based code that computes the radiative transfer process in dusty media. The set-up adopted here is fully described in Behrens et al. (2018), and we summarize it as follows.

The spatial distribution of the light sources is taken from the position of the stellar clusters (particles) in the simulations; for each cluster, we use its metallicity and age to compute the stellar SED, by adopting Bruzual & Charlot (2003) models and a Kroupa (2001) IMF. We adopt 10^7 photon packages per wavelength bin per source, which ensure a good convergence (see Behrens et al. 2018, in particular appendix A). While this is taken as our fiducial model, we note that using different stellar emission models and/or including the nebular continuum can change intrinsic UV broad-band properties by a factor up to $\simeq 20$ per cent (Wilkins et al. 2016).

Dust distribution is taken from the simulations by adopting a fiducial value of $f_d = 0.08$ (Behrens et al. 2018) for the dust-to-metal ratio, i.e. the best fit simultaneously matching the UV and FIR SED of selected high- z galaxies (Laporte et al. 2017a). We also assume a dust composition and grain size distribution reproducing the MW extinction curve (Weingartner & Draine 2001), and a dust emissivity $\beta_d = 2$. The value of f_d and dust composition are uncertain at high z (Wiseman et al. 2017). Note that in the SKIRT runs, we are adopting a f_d value that is 3.75 times higher than the one used in the simulations. In the future, we reserve the option to change such fiducial set-up, e.g. from $f_d = 0.08$ to $f_d \simeq 0.2$ as seen in local galaxies (De Looze et al. 2020), or use the MW $f_d = 0.3$ value (e.g. Hirashita & Ferrara 2002). We use 100 logarithmically spaced spectral bins to cover the $-1 \leq \log(\lambda/\mu\text{m}) \leq 3$ rest-frame wavelength and an additional finer grid of 40 bins at $0 \leq \log(\lambda/\mu\text{m}) \leq 1.5$, i.e. to have a good coverage of the MIR range. Using SKIRT, we compute the scattering and absorption without accounting for dust self-absorption, which can be relevant for column densities of the order of $\gtrsim 10^{24} \text{ cm}^{-2} \mathcal{D}_0/D$, but gives only a minor contribution to the MIR emission in our typical object (Behrens et al. 2018, in particular see appendix A).

Similarly to the emission lines, the continuum data products are spatially resolved spectra.

3 RESULTS

What do SERRA galaxies look like? To have a visual representation, we select nine different $M_\star \sim 10^9 M_\odot$ galaxies in the redshift interval $6 \lesssim z \lesssim 8$, chosen as a showcase of the different evolutionary stages.

In Fig. 1, we plot maps of the gas surface density (Σ_g) of these galaxies, oriented face-on.¹⁷

In a cosmological structure formation scenario, gas starts to condense in overdensities generated by DM haloes; via filamentary accretion in the IGM/CGM, gas flows to the centre of the potential DM well, where it can cool and reach densities high enough that H₂ and thus star formation is possible (upper panels in Fig. 1). Mergers represent landmarks of galaxy evolution, as per the hierarchical build-up scenario, and objects can often be seen in different phases of the merging process (middle panels in Fig. 1). If the galaxy mass is high enough and it is not disturbed by mergers, a spiral structure (Ceverino, Primack & Dekel 2015; Pallottini et al. 2017a) forms within a rotating and pressure-supported disc (Inoue et al. 2016b; Leung et al. 2020), while it continues to accreting gas and forming stars (lower panels in Fig. 1).

The morphological evolution is particularly rapid at high z , as the rate of mergers per unit time and fresh gas accretion is an increasing function of redshift (Fakhouri, Ma & Boylan-Kolchin 2010; Correa et al. 2015). Furthermore, the stellar feedback is particularly violent because of the episodic and bursty nature of the star formation history (Pallottini et al. 2017b; Ma et al. 2018). Thus, the same galaxy can dramatically change its morphology in a relatively short time lapse, i.e. ~ 25 Myr (e.g. Kohandel et al. 2019, fig. 5).

3.1 Stellar build-up

We start the quantitative analysis of SERRA by looking at the formation history of the stellar component of our galaxies.

The stellar mass build-up of galaxies in SERRA is plotted in Fig. 2. The evolution is shown up to $z = 7.7$ for 202 individual galaxies, each one of them being coloured according to the host halo mass.¹⁸ Note that all the galaxies in Fig. 2 are defined via object identification at $z = 7.7$; thus, mass contribution from $z > 7.7$ mergers is included in the evolutionary track.

Galaxies start to form from $z \simeq 18$, when the Universe is $t \simeq 200$ Myr old. In the plotted redshift range, the stellar masses span from 10^6 to $5 \times 10^{10} M_\odot$ and the galaxies have typical metallicity in the range $0.1 \lesssim Z/Z_\odot \lesssim 0.5$ (see also Gelli et al., in preparation). Since the suite is surveying biased regions of the Universe, relatively rare galaxies ($M_\star \gtrsim 10^{10} M_\odot$) are present since $z \lesssim 9$; in particular, 37 targets have $M_\star \geq 10^9 M_\odot$ at $z = 7.7$.

Objects in our sample can be divided into central (left-hand panel of Fig. 2) and non-central (right-hand panel), depending on whether they are the most massive galaxy in the hosting DM haloes. For central galaxies, the higher the DM halo mass, the higher is the formation redshift of the first stellar populations, as a consequence of the hierarchical structure formation process.

For a non-central galaxy, a relation between M_\star and M_h is not expected. Note that non-central galaxies are not necessarily satellites of the most massive galaxy in the hosting DM halo; however, being at a relatively close distance ($\lesssim 20$ kpc), they can be affected by mass

¹⁷We define the face-on orientation by using the total stellar angular momentum. This working definition gives reasonable results even in the case of a close merger.

¹⁸Halo mass definition can be done either by direct summation of particle groups in the halo finder or using a spherical overdensity criterion. Here, as halo mass we adopt ‘M200c’, i.e. integrating the DM mass contained in a sphere centred around the stellar centre of mass up to the radius where the density is 200 times higher than critical density δ_c , i.e. $M_h = \int \rho_{\text{dm}} d^3r = 200\delta_c \int d^3r$. Selecting a different threshold value for the density (e.g. Δ_c from the spherical collapse model or 500) or adopting the matter density instead of the critical density can give differences up to a factor of 3 in the halo mass.

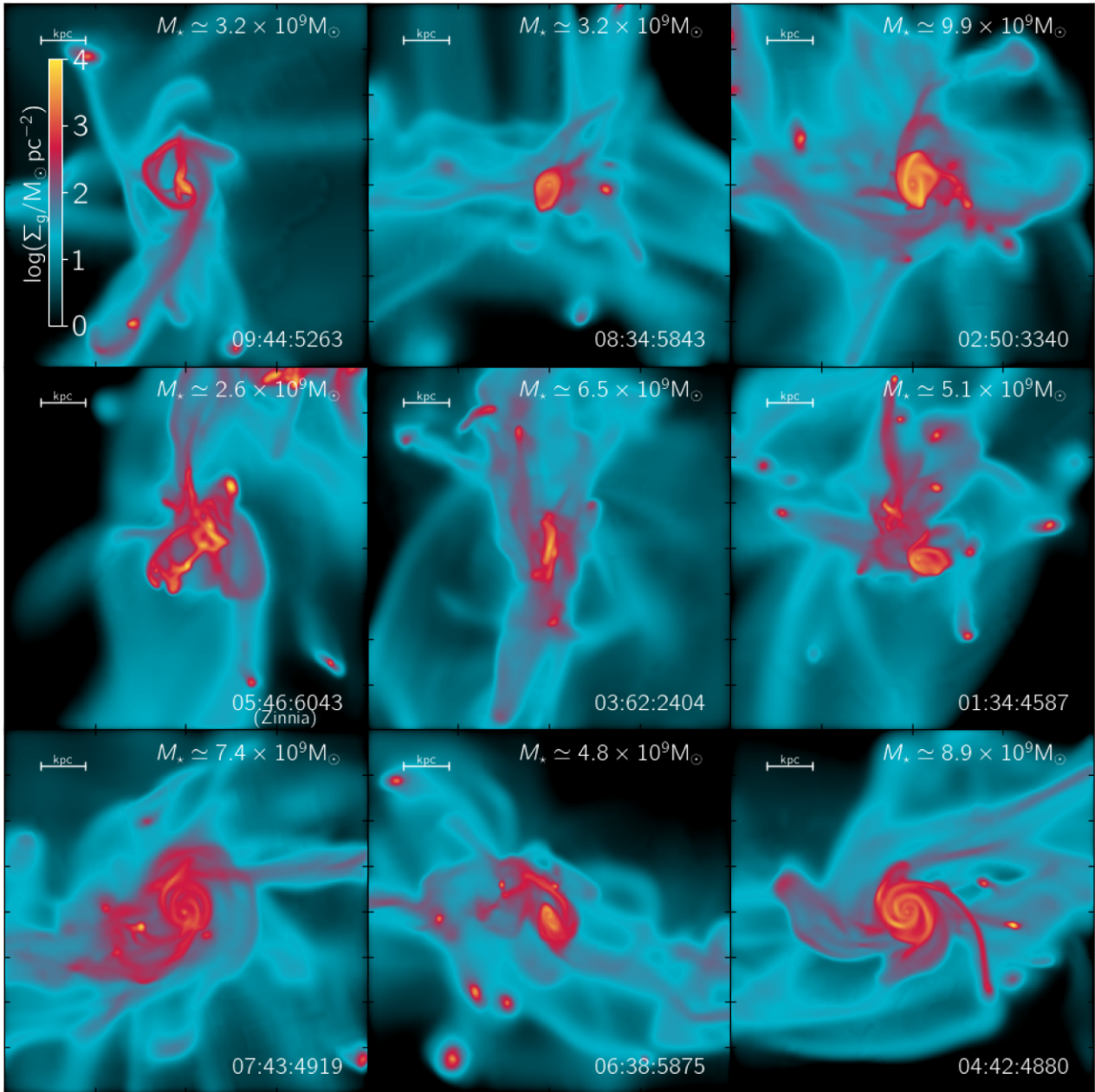


Figure 1. Overview of SERRA galaxies. Each panel shows the gas surface density (Σ_g) of a galaxy with $M_* \sim 10^9 M_\odot$. To give a qualitative overview of the different morphologies found in SERRA, galaxies are taken at $6 \lesssim z \lesssim 8$, each coming from a different simulation in the suite. For each panel, the galaxy stellar mass and identifier (see Section 2.4.1) and name when present are shown in the upper right and lower right parts, respectively.

exchange, metal enrichment, and radiative feedback from the latter. In the following sections, we see that they typically follow similar scaling relations as the central galaxies but with a larger dispersion.

Regardless of the distinction, almost all the galaxies experience a rapid increase of their stellar mass in their first ~ 100 Myr, followed by a less intense growth phase. To have a closer look, we can check their star formation history (Fig. 3). In the left-hand panel, we plot the SFR as a function of galaxy age¹⁹ (t_*). Data for both central and non-central are divided into three groups of 69 targets, depending

¹⁹The galaxy age t_* is defined as the time from the first star formation event; we stress it should be interpreted as time reference more than a galaxy physical property (cf. Tacchella et al. 2018).

on the maximum SFR reached during the history of the galaxy, and each galaxy track is coloured with the stellar mass at $z = 7.7$.

During the first 400 Myr, galaxies with $M_* \lesssim 10^7 M_\odot$ typically have $\text{SFR} \lesssim 5 M_\odot \text{yr}^{-1}$, intermediate-mass galaxies ($10^8 \lesssim M_* \lesssim 10^9 M_\odot$) wiggle around $\text{SFR} \simeq 10 M_\odot \text{yr}^{-1}$, while $M_* \gtrsim 10^9 M_\odot$ have $\text{SFR} \simeq 30 M_\odot \text{yr}^{-1}$ for long spans of times, and can reach peaks of $\text{SFR} \sim 200 M_\odot \text{yr}^{-1}$ during short bursts. The majority of bursts during the galaxy history have time-scales of the order of $\simeq 10$ Myr: A peak in SFR activity determines a delayed peak of stellar feedback, which temporarily suppresses the star formation (see Pallottini et al. 2017a, for more details regarding the feedback impact). Such suppression typically becomes a temporary quenching in low-mass galaxies (Gelli et al. 2020). More details on this effect are given later on. Note that extreme variations – bursts of the order of

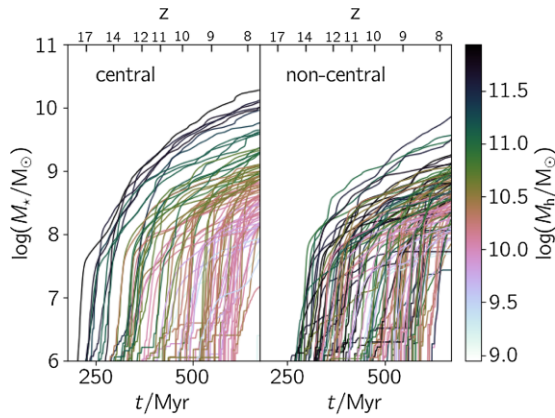


Figure 2. Cumulative stellar mass (M_*) as a function of cosmic time (t) in the SERRA simulation. Galaxies are divided into central (89 objects, left-hand panel) and non-central (113 objects, right-hand panel), depending on whether they are the most massive galaxy in the host DM halo. For each of the 202 galaxies, the evolutionary track is coloured (see the colour bar) according to the host halo mass¹⁸ at $z = 7.7$. The redshift (z) corresponding to t is indicated in the upper axis.

$10 \times$ the time-averaged value – are likely induced by merger events and massive inflow of new fresh gas.

3.2 Main sequence

It is interesting to look at the history in the SFR– M_* plane, i.e. the ‘main sequence’, that is shown in the right-hand panel of Fig. 3. Galaxies in SERRA start their life with a specific star formation rate $s\text{SFR} \equiv \text{SFR}/M_* \simeq 100 \text{ Gyr}^{-1}$ and gradually move to $s\text{SFR} \simeq 10 \text{ Gyr}^{-1}$ as they grow older (around $t_* \simeq 200 \text{ Myr}$; see also Pallottini et al. 2017b). As expected from the $s\text{SFR}$ evolution (see Madau & Dickinson 2014, and reference within), galaxies in the EoR have extreme values with respect to what observed locally ($z = 0$, $s\text{SFR} \simeq 0.1 \text{ Gyr}^{-1}$) and at low redshift ($z \simeq 1$, $s\text{SFR} \simeq 1 \text{ Gyr}^{-1}$). The values reported for $M_* \simeq 10^9 M_\odot$ galaxies in SERRA are in good agreement with those observed at $z \sim 7$ (González et al. 2010; Stark et al. 2013). Moreover, $z \simeq 6$ observations by Jiang et al. (2013) show that young (old) galaxies have $s\text{SFR} = \text{SFR}/M_* = 39.7 \text{ Gyr}^{-1}$ (4.1 Gyr^{-1}), i.e. hinting at a decreasing trend of $s\text{SFR}$ with galaxy age. Direct comparison with the data from Jiang et al. (2013) reveals that the general trends from the stellar tracks of SERRA galaxies well reproduce the observations of old galaxies. However, we find $s\text{SFR} = 39.7 \text{ Gyr}^{-1}$ for young $M_* \simeq 10^9 M_\odot$ galaxies only during bursty periods. Bimodality in the M_* –SFR plane has been probed by observations of large samples up to $z \lesssim 6$ by Rinaldi et al. (2021); however, the authors show that ILLUSTRISTNG50 simulations (Pillepich et al. 2019) struggle to reproduce the starburst cloud at any redshift interval. Further and more refined analysis will be needed in order to quantify if this lack is due to intrinsic limitations in the simulations or to a bias in the comparison (e.g. because of the volume).

3.3 Halo-to-stellar mass relation

Here, we focus our analysis at $z = 7.7$ and we start by looking at the halo mass-to-stellar mass relation, which is often used as a benchmark for the efficiency of star formation. The relation for central galaxies in SERRA is presented in Fig. 4. At $z = 7.7$, the halo masses range from about 10^9 to $5 \times 10^{11} M_\odot$ and the stellar mass of

central galaxies from about 10^6 to $5 \times 10^{10} M_\odot$. A few objects with mass of $\simeq 10^6 M_\odot$ are present, as most of them are embedded in haloes hosting more massive galaxies, while smaller objects are not identified as galaxies, because of the threshold of 20 stellar particles adopted in the definition (see Section 2.4.1).

In the same figure, we compare with the results from abundance matching models (Behroozi et al. 2013c, 2019; Moster et al. 2013, 2018) and the M_* – M_h from numerical simulations (Xu et al. 2016; Ma et al. 2018).

The central galaxies in SERRA have an average trend that is in broad agreement with the M_* – M_h from Behroozi et al. (2013c). Notably, the redshift-dependent turnover at $M_h \sim 10^{11} M_\odot$, corresponding to the turnover at L_* in the luminosity function, is well reproduced. The SERRA predictions diverge from the Behroozi et al. (2013c) curve at $M_h \lesssim 5 \times 10^{10} M_\odot$: Most of the galaxies show a larger stellar mass, with a few blatant outliers that sit well below it. Qualitatively, a similar behaviour is found when comparing with Moster et al. (2013), although at $z = 7.7$ there is a disagreement at more than 1σ around $M_h \sim 10^{11} M_\odot$ between Moster et al. (2013) and Behroozi et al. (2013c); such a disagreement is mainly due to the different assumption in the abundance matching models and the different extrapolation methods (see also Behroozi & Silk 2015; Moster et al. 2018). In particular, for $M_h \lesssim 10^{10} M_\odot$ and at $z \gtrsim 6$, Behroozi et al. (2013c) should be taken with care, since results in that range have been extrapolated due to the lack of data. The situation is qualitatively similar also by considering updated versions of the abundance matching models (Moster et al. 2018; Behroozi et al. 2019).

Despite these caveats, in this work, we take the M_* – M_h from Behroozi et al. (2013c) as a reference. With this consideration in mind, it seems that feedback at the low-mass end in SERRA is too weak to suppress star formation significantly and/or the lack of resolution to solve the mini-halo progenitors is spoiling the evolution of low-mass galaxies.

As Behroozi et al. (2013c) is broadly consistent with the relation from Ma et al. (2018), similar considerations hold for the comparison between SERRA and FIRE-2. However, note that the latter reports no redshift evolution for the M_* – M_h , while – particularly at high redshift – there is a rapid evolution in the M_* – M_h from Behroozi et al. (2013c). In the low-mass end, results from SERRA are closer to what is reported by RENAISSANCE as analysed in Xu et al. (2016); note that we report the fit from Xu et al. (2016) extrapolating at $M_h > 10^{10} M_\odot$, so extra care should be taken in looking at the high-mass end from RENAISSANCE.

To summarize, while at high M_h the SERRA results are consistent with different models, at low M_h they generally favour larger stellar masses with respect to the extrapolated predictions. How can we understand such a trend?

3.3.1 Low-mass galaxies: interpreting their trend

To answer this question, consider the star formation history (Fig. 5) of ‘Alyssum’, a typical central, low-mass ($M_* \simeq 5 \times 10^8 M_\odot$) SERRA galaxy²⁰ at $z = 7.7$. Alyssum does not experience any major merger down to $z = 7.7$. Its first star formation event occurs in an almost

²⁰Note that for the analysis of Alyssum, we relax the threshold of a minimum 20 particles to define a galaxy: For snapshot prior to the first identification of the galaxy with ROCKSTAR, we backtrack each single star particle to the first formation event.

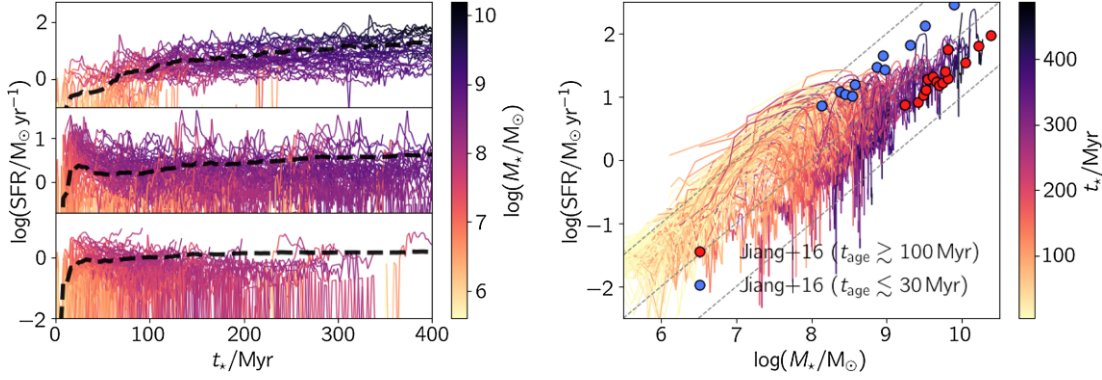


Figure 3. Star formation history in SERRA. Left-hand panel: SFR as a function of stellar age¹⁹ (t_*). Each galaxy track is coloured with M_* at $z = 7.7$. The data are divided into three samples: a galaxy is in the upper panel if $\text{SFR} > 13.8 M_\odot \text{ yr}^{-1}$ at least once during its history, in the middle panel if $\text{SFR} \gtrsim 4.8 M_\odot \text{ yr}^{-1}$, in the lower panel otherwise. Limits are chosen such that each panel contains about 67 galaxies. The SFR average for each sub-sample is shown by the black dashed line in each panel. Individual SFRs (averages for each sub-sample) are computed over a period of 2 Myr (10 Myr). Right-hand panel: evolution of SFR versus M_* . Each galaxy is coloured with its age as it increases with M_* . Crosses are the observations from Jiang et al. (2013) with the sample divided into young and old galaxies. The three dashed lines indicate a constant value of $\text{sSFR} \equiv \text{SFR}/M_* = 1, 10, 100 \text{ Gyr}^{-1}$. The sSFR has been averaged over 20 Myr to reduce flickering effects.

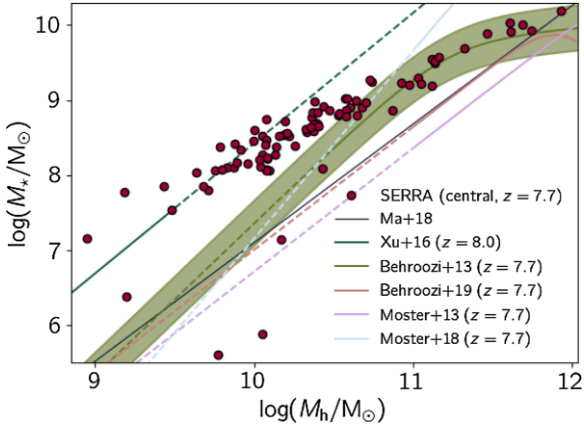


Figure 4. Halo-to-stellar mass (M_h – M_*) relation for 89 simulated central galaxies at $z = 7.7$. We overplot the results from other numerical simulations from RENAISSANCE (Xu et al. 2016, at $z = 8$) and FIRE-2 (Ma et al. 2018, redshift independent fit), along with the results from different abundance matching models (Behroozi & Conroy 2013c; Moster, Naab & White 2013, 2018; Behroozi et al. 2019) at the same redshift. Dashed lines indicate the M_h ranges where models are extrapolated. In this work, Behroozi et al. (2013c) is the reference for comparisons, and the shaded region shows the standard deviation.

pristine ISM at $z \simeq 14$, when the galaxy halo mass is $M_h \simeq 10^9 M_\odot$ or $T_{\text{vir}} \simeq 10^4 \text{ K}$.

In the first burst, a $M_* \simeq 5 \times 10^5 M_\odot$ stellar cluster is formed; the star formation is completely quenched for a time span of 200 Myr thereafter. The metallicity rapidly rises from the initial floor value of $Z = 10^{-3} Z_\odot$ to $Z \simeq 10^{-2} Z_\odot$, and subsequently slowly decreases because of the onset of a powerful outflow, and – most prominently – cosmological accretion of fresh gas.

Quenching of star formation is due to radiative feedback. Initially, the mean intensity of the H_2 photodissociating radiation field²¹ produced by the newly born stars is very high, $\langle G \rangle = 10^3 G_0$ (see the lower panel of Fig. 5). This is well above the critical threshold

²¹ $G_0 = 1$ roughly corresponds to $J_{21} = 100$, where J_{21} is the radiation intensity in units of $10^{-21} \text{ erg s}^{-1} \text{ cm}^{-2} \text{ Hz}^{-1} \text{ sr}^{-1}$.

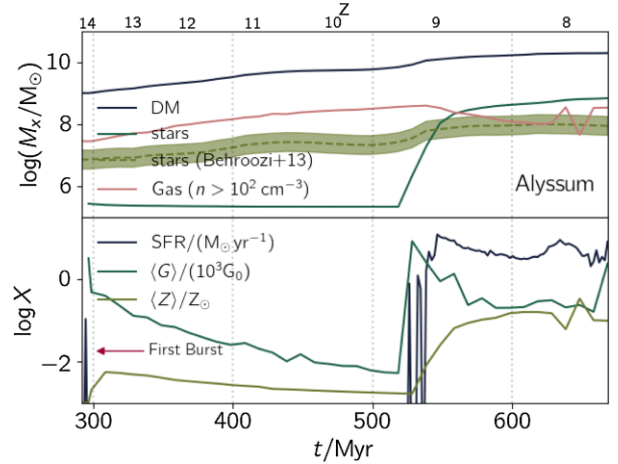


Figure 5. Evolutionary history of ‘Alyssum’, a $M_* \simeq 5 \times 10^8 M_\odot$ SERRA galaxy at $z = 7.7$. Upper panel: DM, stellar, and dense gas ($n > 10^2 \text{ cm}^{-3}$) mass as a function of cosmic time and corresponding redshift; for reference, we add the evolution of $M_*(M_h, z)$ from Behroozi et al. (2013c). Lower panel: SFR, average Habing radiation field (G), and gas metallicity (Z). Note that the both SFR and M_* are computed with a $\Delta t = 2 \text{ Myr}$ time sampling, while the other quantities have a coarser $\Delta t \simeq 10 \text{ Myr}$ sampling, due to availability of simulation snapshots.

for H_2 formation in a pristine environment, $\langle G^* \rangle \simeq 10 G_0$ (Johnson, Dalla & Khochfar 2013). Thus, the galaxy cannot form stars until the ISRF decreases below this threshold, roughly 200 Myr after the burst. In this first phase, M_* is below the (extrapolated) Behroozi et al. (2013c) relation.

When star formation is reignited, the process repeats with increasingly shorter cadence. This is due to the fact that metals and dust produced by the SNe improve the self-shielding ability of the gas, thereby enabling H_2 formation even in the presence of a supercritical ISRF intensity. After two additional bursts, the star formation stabilizes to $\simeq 10 M_\odot \text{ yr}^{-1}$, and steadily continues in spite of the very strong, $\langle G \rangle \simeq 100 G_0$, ISRF. The metallicity has overtaken the $Z = 10^{-2} Z_\odot$ level, which we can therefore empirically identify as the minimum metallicity required to sustain a continuous star formation activity. At that point, the galaxy shortly overshoots the

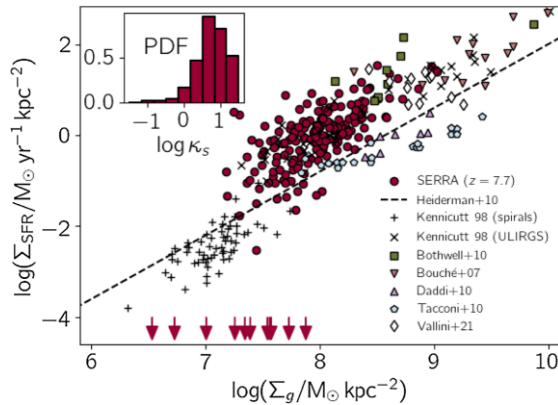


Figure 6. Schmidt–Kennicutt relation at $z = 7.7$. We plot the ‘classical’ relation (Krumholz 2015), i.e. star formation, Σ_{SFR} , versus gas, Σ_g , surface density. The data from SERRA are marginally resolved, i.e. we smoothed the maps of both Σ_{SFR} and Σ_g with a Gaussian kernel with a width of 0.5 kpc and take the maximum/central values in the maps, in order to have a uniform sample. For the 11 objects that are temporarily quenched at $z = 7.7$ (see Section 3.3), we show upper limits (red arrows). We also report the values observed at $z = 0$ for spirals and ultraluminous infrared galaxies (ULIRGs; Kennicutt 1998), for ULIRGs and sub-millimetre galaxies (Bothwell et al. 2010), for low-redshift ($1 \lesssim z \lesssim 2$) galaxies (Bouché et al. 2007; Daddi et al. 2010; Tacconi et al. 2010), and inferred from high-redshift ($z > 5.5$) targets (Vallini et al. 2021, see the text for details). The dashed line is the Heiderman et al. (2010) fit to Kennicutt (1998), reported in equation (9). As an inset, we add the probability distribution function (PDF) of the burstiness parameter (κ_s , equation 10) for galaxies in SERRA.

Behroozi et al. (2013c) M_\star – M_h curve. This situation is however transient: More massive galaxies later on fall back on the M_\star – M_h (Fig. 4).

The described trend crucially depends on the assumption that star formation occurs in MCs. We cannot exclude that a different star formation mode, occurring in dense – but not necessarily molecular – gas (e.g. Semenov et al. 2016; Lupi et al. 2018), might be at work in early galaxies. In such case, the quenching phase could be shorter or even completely absent. The quenching details and duration might also depend on mass resolution, although the physical arguments derived from the simulation analysis should hold anyway. We will explore these possibilities in future work.

3.4 Schmidt–Kennicutt relation

The Schmidt–Kennicutt (KS) relation for SERRA galaxies is plotted in Fig. 6. We find that simulated galaxies are typically located *above* the local relation (Heiderman et al. 2010)

$$\Sigma_{\text{SFR}}^{\text{KS}} = 10^{-12} (\Sigma_g / \text{M}_\odot \text{kpc}^{-2})^{1.4} \text{M}_\odot \text{yr}^{-1} \text{kpc}^{-2}, \quad (9)$$

which is a fit to the Kennicutt (1998) observations.

Note that 11 galaxies are temporarily quenched at $z = 7.7$, as discussed in the previous section. Observations of both local starbursts (Kennicutt 1998; Bothwell et al. 2010) and $1 \lesssim z \lesssim 2$ galaxies (Bouché et al. 2007; Daddi et al. 2010; Tacconi et al. 2010) match our results quite well.

The deviation from the KS can be quantified via the ‘burstiness’ parameter (Ferrara et al. 2019; Pallottini et al. 2019)

$$\kappa_s \equiv \Sigma_{\text{SFR}} / \Sigma_{\text{SFR}}^{\text{KS}}, \quad (10)$$

which also governs the observability of several emission lines (Vallini et al. 2020, 2021). At $z = 7.7$, galaxies in SERRA have an average value of $\kappa_s = 3.03_{-1.8}^{+4.9}$.

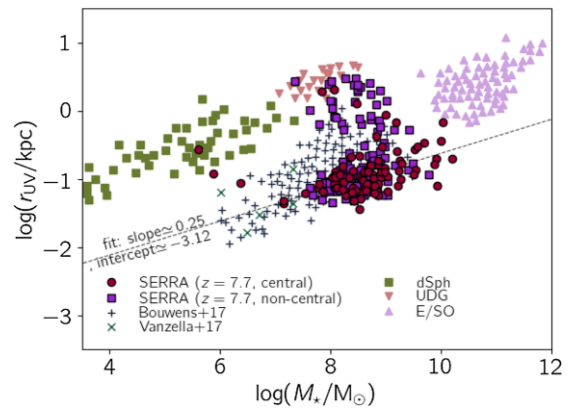


Figure 7. Size–stellar mass relation. The size of SERRA galaxies is taken to be equal to r_{UV} , the radius encompassing 50 per cent of the UV luminosity. As indicated in the legend, we distinguish between central and non-central galaxies at $z = 7.7$. As an inset, we overplot the fit for the central galaxies in SERRA, obtained by excluding the outliers due to mergers (see equation 11). We report the observations for $6 \leq z \leq 8$ lensed galaxies (Bouwens et al. 2017) and ‘proto-globular’ clusters at $z \gtrsim 3$ (Vanzella et al. 2017, 2019). We also show data for a collection of local galaxies (Brodie et al. 2011; Norris et al. 2014): dSphs, UDGs, and E/S0.

Unfortunately, CO detections (D’Odorico et al. 2018; Pavese et al. 2019) in EoR galaxies are rather difficult and rare, making a precise assessment of the gas mass rather uncertain, albeit indirect methods (e.g. Zanella et al. 2018, that propose to use [C II] as a proxy for molecular gas) might overcome such problem. An alternative possibility consists of combining [C II] and C III lines to determine κ_s , the gas density, and metallicity (Vallini et al. 2020, see also Ferrara et al. 2019 for details on the physical model). This method has been applied to COS-3018 ($z = 6.854$), the only normal EoR galaxy so far detected in both [C II] (Smit et al. 2018, see Carniani et al. 2018a for the size determination) and C III (Laporte et al. 2017b). Vallini et al. (2020) infer $\kappa_s \simeq 3$ for COS-3018, in line with the average value from SERRA.

Using a similar approach, but based instead on the FIR [C II] and [O III] lines, Vallini et al. (2021) find $\kappa_s \simeq 36.3_{-18.7}^{+19.1}$ for 10 $z > 5.5$ galaxies. This value is in line with the values found for SERRA galaxies with approximately $\Sigma_g \simeq 10^9 \text{M}_\odot \text{kpc}^{-2}$.

3.5 Size–stellar mass relation

The size–stellar mass relation for our sample is reported in Fig. 7. We define the galaxy size, r_{UV} , as the radius that contains 50 per cent of the UV luminosity.²² In our sample, the behaviour is twofold: Most of the galaxies have $r_{\text{UV}} \simeq 100$ pc, while about 10 per cent of the objects have larger sizes ($\simeq 1$ kpc). The latter group is composed of galaxies – mostly non-central – that have recently experienced or are experiencing a merger (e.g. see later in Fig. 9). While their size–stellar mass relation resembles that of local ultradiffuse galaxies (UDGs; Brodie et al. 2011; Norris et al. 2014), this might be a transient feature related to the merging phase. Fitting the relation for the central SERRA galaxies excluding the mergers, we obtain

$$\log \frac{r_{\text{UV}}}{\text{kpc}} = (0.249 \pm 0.002) \log \frac{M_\star}{\text{M}_\odot} - 3.12 \pm 0.13. \quad (11)$$

²²In simulations for which the continuum radiative transfer is not available, it is common to adopt the 50 per cent or 80 per cent stellar mass radius. With respect to r_{UV} , this choice underestimates the size by a factor of a few, since UV scattering, which depends on the dust distribution, is not accounted for.

The size–stellar mass relation from SERRA has a slope consistent with the corresponding one in the local universe encompassing dwarf spheroidals (dSphs), UDGs, and elliptical/lenticular (E/S0); however, in SERRA, the relation is offset by about an order of magnitude, qualitatively as expected from the redshift evolution (Shibuya, Ouchi & Harikane 2015).

Our data are broadly consistent with that derived by Bouwens et al. (2017) for $6 \leq z \leq 8$ lensed galaxies and by Vanzella et al. (2019) for $z \gtrsim 3$ for ‘proto-globular’ clusters. However, the median value of the simulated relation is downshifted by a factor of $\simeq 2$ with respect to Bouwens et al. (2017) data. The reasons for this discrepancy are uncertain, but they might be related to the feedback prescriptions adopted in SERRA. For example, it might be that the energy deposition is insufficient to drive a sufficient amount of gas away from the galactic centre. While the main goal of all feedback models is to primarily prevent excessive star formation, the resulting kinematic behaviour may considerably differ among them (see Rosdahl et al. 2017, for an in-depth study).

For example, a feedback based on delayed cooling, which shares many of the features of the physically motivated feedback implemented in SERRA, tends to puff up the gas distribution. A kinetic feedback, instead, is known to promote powerful outflows. Intriguingly, though, in Lupi et al. (2020), we adopted a kinetic feedback prescription following Hopkins et al. (2018), and the same ICs to model the galaxy Freesia presented in Pallottini et al. (2019). By comparing the two simulations, we find a difference of only a few per cent in terms of the galaxy size.

Alternatively, part of the tension might be alleviated by properly considering observational uncertainties. As shown in Zanella et al. (2021), depending on the band and the resolution of the synthetic observation, we can expect that adopting a realistic instrumental noise for the simulated data can give a $\simeq 20$ per cent error on the recovery of r_{UV} . This error estimate for the mass–size relation is likely to be a lower limit, since in Zanella et al. (2021) we consider neither lensing model uncertainties nor stellar mass determination errors. Further study on the size–mass relation and a full morphological analysis are left for future work.

3.6 Emission properties

Before presenting statistical results for the entire SERRA sample at $z = 7.7$, we want to focus on the specific cases of 02 : 46 : 3788 and 05 : 46 : 6043, which are also known as ‘Dianthus’ and ‘Zinnia’, respectively.

Both Dianthus and Zinnia have similar stellar masses ($M_\star = 2.53 \times 10^9$ and $2.19 \times 10^9 M_\odot$), SFRs (11.13 and $24.46 M_\odot \text{ yr}^{-1}$), and both are moderately bursty ($\kappa_s = 8.46$ and 4.29), i.e. within about the average of the survey.

The main emission properties of Dianthus and Zinnia are shown in Figs 8 and 9, respectively.²³ For the two, the morphology is very different: While Dianthus appears as a regular star-forming galaxy, Zinnia has just experienced a merger (a very common situation at these high redshifts), and its stars/gas are still in the relaxation process (see Fig. 1).

Dianthus has a single peak for both continuum and line emission. The stellar component has a radius of $\simeq 0.1$ kpc, with the UV

being slightly less concentrated than the IR continuum. Instead, both the [C II] and the [O I] – tracing the gas distribution – have typical radii of $\simeq 0.4$ kpc, i.e. with a Perito ratio ($r_{[\text{CII}]} / r_{\text{UV}}$) similar to what is observed for high- z targets (Carniani et al. 2018a) but not as extreme as for the [C II] haloes observed for galaxies with higher masses (Fujimoto et al. 2020; Ginolfi et al. 2020). The [O III], being linked to the ionization parameter, is much more concentrated. The morphology of Zinnia appears elongated, with a maximum extension of about 1.5 kpc; three main components are clearly visible in the IR continuum ($\Sigma_{\text{IR}} \gtrsim 10^{12} L_\odot \text{ kpc}^{-2}$), and in various FIR lines ($\Sigma_{\text{line}} \gtrsim 5 \times 10^9 L_\odot \text{ kpc}^{-2}$, for [C II], [O I], and [O III]). The FIR line emission from different ions is mostly co-spatial for Zinnia, with a few noticeable differences. While [C II] and [O I] trace similar gas phases, the [O I] is more concentrated and shows higher surface brightness in the three main components ($\Sigma_{[\text{OI}]} \simeq 5 \times 10^{10} L_\odot \text{ kpc}^{-2}$). The [C II] is instead fainter at the peaks ($\Sigma_{[\text{CII}]} \simeq 10^{10} L_\odot \text{ kpc}^{-2}$) but brighter in the outskirts. The [O III] emission is particularly intense ($\Sigma_{[\text{OIII}]} \simeq 5 \times 10^{10} L_\odot \text{ kpc}^{-2}$) and extended, making it the most luminous line, i.e. $L_{[\text{OIII}]} \simeq 5L_{[\text{CII}]}$ $\simeq L_{[\text{OI}]}$. Note that for both galaxies, the luminosity of [C II], [O I], and [O III] is within the observed scatter for local dwarf galaxies with similar SFR (De Looze et al. 2014).

In Dianthus and Zinnia, all these prominent star-forming knots are not visible in the UV, because these regions are significantly obscured ($\tau_V \gtrsim 5$). On average, though, both galaxies are basically transparent, with $\langle \tau_V \rangle \simeq 0.61$. Interestingly, such a large optical depth is caused by a relatively little amount of dust ($M_d \sim 10^5 M_\odot$) distributed in a compact region around the star-forming sites. As a result of such geometry, the dust becomes hot.

In particular, the SED-fitted temperature is $T_{\text{SED}} \simeq 88$ K for Zinnia (Sommovigo et al. 2021). However, the mass-weighted temperature is lower, $\langle T_d \rangle_M \simeq 61.8$ K, and T_{SED} is skewed towards the luminosity-weighted temperature of $\langle T_d \rangle_L \simeq 117.3$ K. The latter is boosted by the aforementioned pockets of dust around active star-forming regions (already noted in Behrens et al. 2018), which therefore produce a blatant MIR excess over a standard grey-body spectrum. We warn that such large temperatures might be partially an artefact of numerical resolution; we defer the discussion of this issue to Section 3.6.2.

The emission properties of Zinnia (such as e.g. luminosity and surface brightness ratios, value for the luminosity of different tracers with SFR) are pretty typical of galaxies in SERRA. However, the morphological properties (extent of the line emission, multicomponent emission) are highly disturbed by the merger episode. For observations of such multicomponent galaxies, single-zone assumptions and usual calibrators (e.g. IRX- β relation) adopted to infer their properties should be taken with care, as detailed in Ferrara et al. (2022) for the analysis of REBELS galaxies (Bouwens et al. 2021).

In the next sections, we turn to the discussion of the entire galaxy sample.

3.6.1 UV production

To quantify the production of UV photons by SERRA galaxies, we introduce the commonly adopted (Madau & Dickinson 2014) conversion factor \mathcal{K}_{1500} , defined by

$$\text{SFR} \equiv \mathcal{K}_{1500} L_{1500}. \quad (12)$$

Observationally, \mathcal{K}_{1500} is a particularly relevant quantity, since it can be used to infer the SFR from the UV data (e.g. Kennicutt & Evans 2012; Madau & Dickinson 2014). In general, \mathcal{K}_{1500} depends

²³Here, we focus on face-on views of the systems; however, we note that morphology and inclination can be important factors in determining the spectral shape and observed properties of galaxies (Behrens et al. 2018; Katz et al. 2019; Kohandel et al. 2019).

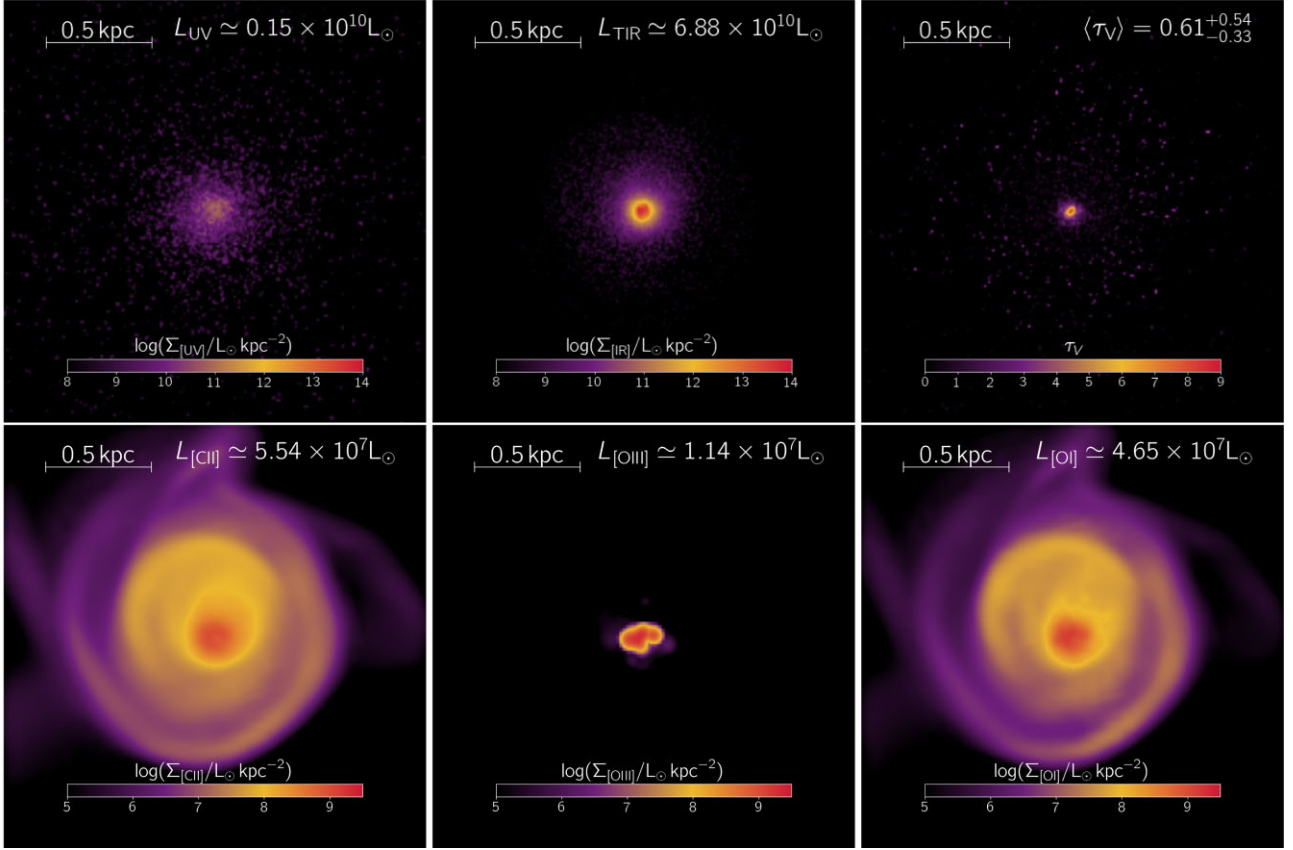


Figure 8. Emission properties of ‘Dianthus’, a $M_* = 2.53 \times 10^9 M_\odot$ star-forming galaxy in SERRA ($z = 7.7$). The upper panels show the continuum properties: the surface brightness in the rest-frame UV (left-hand panel, Σ_{UV} , $1000 \leq \lambda/\text{\AA} \leq 3000$), in the total IR emission (centre panel, Σ_{TIR} , $8 \leq \lambda/\mu\text{m} \leq 1000$), and the V-band optical depth (right-hand panel, τ_V). The lower panels show the surface brightness of a set of FIR emission lines: [C II] (left-hand panel, $158 \mu\text{m}$), [O III] (centre panel, $88 \mu\text{m}$), and [O I] (right-hand panel, $61 \mu\text{m}$). The maps are taken in an FOV of 2 kpc with a face-on orientation. As insets, we report the total luminosity of each emission map and the average value of τ_V . Models for line and continuum emission are described in Sections 2.4.2 and 2.4.3, respectively.

on the IMF of the stellar population, its metallicity, and SFR history (SFRh). In the left-hand panels of Fig. 10, we show the distribution of \mathcal{K}_{1500} for the 202 SERRA galaxies, by using the intrinsic (i.e. unattenuated) L_{1500} value and computing the SFR in the last 20 Myr. Both distributions for low ($M_* < 10^9 M_\odot$) and high ($M_* \geq 10^9 M_\odot$) stellar masses show a central wide peak, while the tail is skewed at high (low) \mathcal{K}_{1500} values for the low (high) masses.²⁴

The average is $\langle \mathcal{K}_{1500} \rangle = 1.53^{+0.15}_{-0.13} (1.44^{+0.14}_{-0.09}) \times 10^{-10} M_\odot \text{yr}^{-1} L_\odot^{-1}$ for the low (high) stellar mass subsample. For the full sample, we find instead $\langle \mathcal{K}_{1500} \rangle = 1.52^{+0.16}_{-0.14} \times 10^{-10} M_\odot \text{yr}^{-1} L_\odot^{-1}$. The above mean values are very close to the predictions ($\mathcal{K}_{1500} = 1.47 \times 10^{-10} M_\odot \text{yr}^{-1} L_\odot^{-1}$) from a Kroupa (2001) IMF with $Z_* = Z_\odot$, stellar age $t_* > 300$ Myr, and constant SFR (Madau & Dickinson 2014). Although this might appear as a trivial result, given that a Kroupa (2001) IMF is also assumed in SERRA, the situation requires a deeper inspection.

In the right-hand panel of Fig. 10, we show the dependence of \mathcal{K}_{1500} from the SFRh. We calculate \mathcal{K}_{1500} for a Kroupa (2001) IMF with $Z_* = Z_\odot$ and selecting an exponential function as a representative history, i.e. $\text{SFR}(t_*) \propto \exp(t_*/t_0)$. We allow increasing and decreasing SFRh by changing the time-scale t_0 : Increasing

(decreasing) SFRh has a larger (lower) \mathcal{K}_{1500} value with respect to a constant SFR, as newly formed stars weight more in the \mathcal{K}_{1500} computation. Generally, SERRA galaxies feature a time-increasing SFRh (Fig. 3); however, the increase seen in the range of \mathcal{K}_{1500} is relatively modest ($\simeq 30$ per cent), particularly for $M_* \geq 10^9 M_\odot$ galaxies, since their equivalent time-scale is $t_0 \sim 30$ Myr (see fig. 2 in Pallottini et al. 2017b). The frequent bursts experienced by SERRA galaxies determine the spread of the \mathcal{K}_{1500} PDF at higher and lower values around the mean, as a consequence of the sudden increase of the SFR and subsequent quenching due to stellar feedback, respectively. As a note of caution, while the difference between constant and exponentially increasing SFRh is relatively modest because of the expected value for t_0 from SERRA, assuming a decreasing SFRh for an SED fitting of a galaxy with an increasing SFRh can give a factor of 4 variation in the SFR determination (see also Behrens et al. 2018).

3.6.2 Continuum properties

From the spectra of SERRA galaxies, we compute²⁵ $\text{IRX} \equiv L_{TIR}/L_{UV}$, and the slope of the UV spectrum β in the range (1600–2500) Å. The

²⁴For the PDF \mathcal{K}_{1500} , we show the distinction between high- and low-mass galaxies, since calculating the PDF for central and non-central galaxies gives negligible differences.

²⁵In computing the IRX, we use a UV luminosity integrated in the 1000–3000 Å band. The differences with the often adopted monochromatic luminosity $\lambda_{1600} L_{1600}$ at 1600 Å are within few per cent.

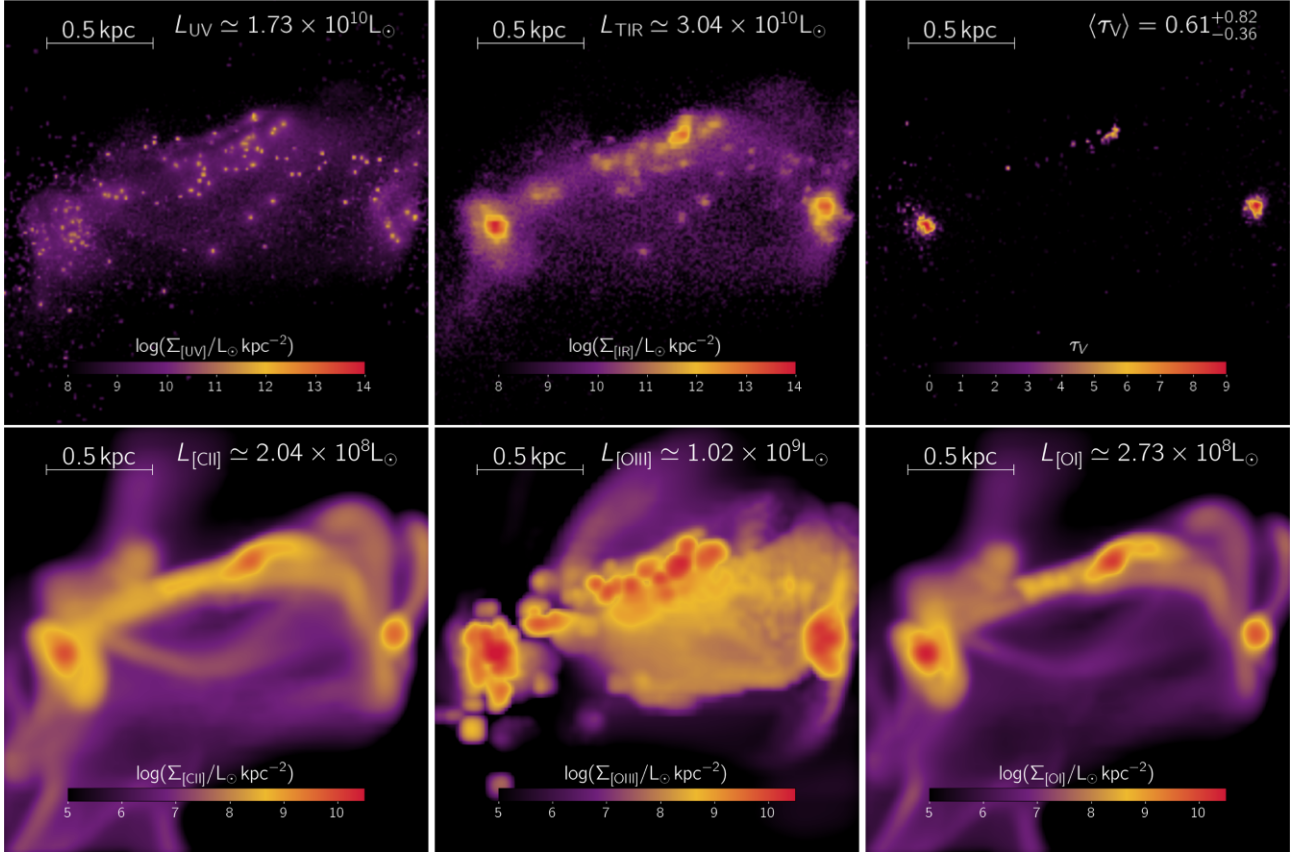


Figure 9. Emission properties of ‘Zinnia’, a $M_* = 2.19 \times 10^9 M_\odot$ merging galaxy in SERRA ($z = 7.7$). Notation as in Fig. 8.

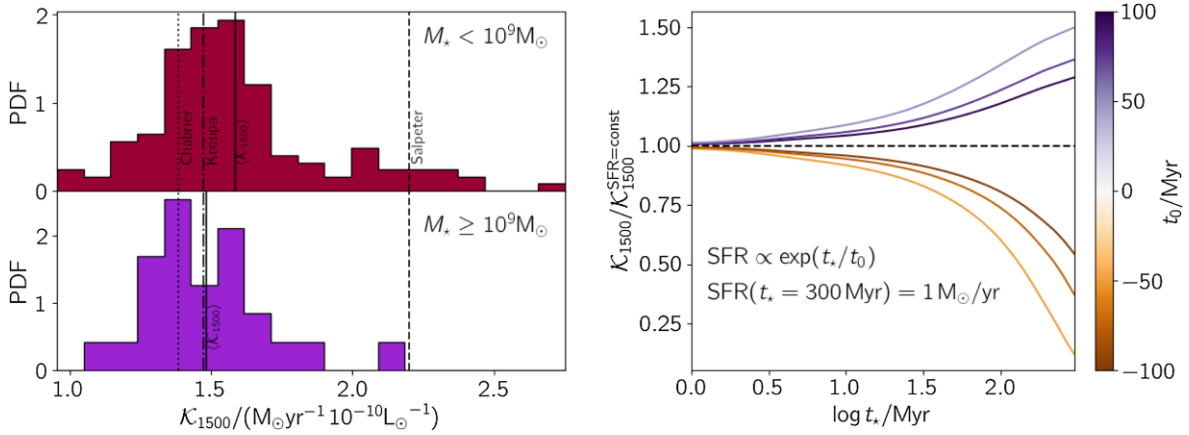


Figure 10. UV–SFR conversion factor (\mathcal{K}_{1500} , equation 12). Left-hand panel: distribution of the \mathcal{K}_{1500} in SERRA. We separately plot the \mathcal{K}_{1500} PDF for galaxies of low ($M_* \leq 10^9 M_\odot$, upper panel) and high ($M_* \geq 10^9 M_\odot$, lower panel) stellar mass. The average of the two sub-samples is plotted with a vertical black solid line. As a reference, we plot as vertical lines the values expected for *constant* star formation histories of stellar population with $Z_* = Z_\odot$, age $t_* > 300$ Myr in the $0.1\text{--}100 M_\odot$ range for Salpeter (1955), Kroupa (2001), and Chabrier (2003) IMFs. Right-hand panel: variations of \mathcal{K}_{1500} due to different star formation history (SFRh). SFRh are exponential functions parametrized by t_0 (see text), as shown in the colour bar. For each SFRh, as a function of the age, we plot \mathcal{K}_{1500} normalized by the value for a constant SFRh. All SFRh have $\text{SFR} = 1 M_\odot \text{yr}^{-1}$ at 300 Myr. For reference, we plot with a dashed line the value for a constant SFRh ($t_0 = \pm\infty$).

IRX– β relation is a convenient summary diagnostic that accounts for the relative balance between UV and FIR photons (Calzetti, Kinney & Storchi-Bergmann 1994; Meurer et al. 1995). The results are presented in Fig. 11, along with high-redshift detections and upper limits.

The bulk of SERRA galaxies have $-2.5 < \beta < -1$, as expected from a stellar population dominated by relatively unobscured, young stars. However, their IRX is typically ~ 10 , as expected from evolved and obscured systems. This apparent contradiction is easily understood as follows. To form stars, the gas must be able to self-shield from the

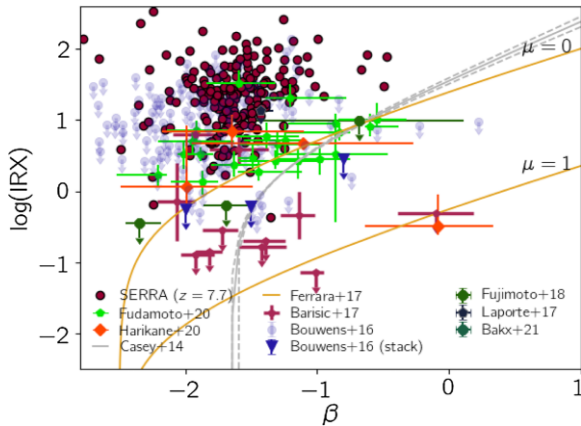


Figure 11. IRX– β relation for $z > 5$ galaxies compared with SERRA galaxies. Data points refer to upper limits (Bouwens et al. 2016; Fujimoto et al. 2017) and detections (Barisic et al. 2017; Laporte et al. 2017a; Fudamoto et al. 2020; Harikane et al. 2020; Bakx et al. 2021). Also shown is same relation for local galaxies (Casey et al. 2014), and that expected from a theoretical work (Ferrara et al. 2017). For the latter, we show the two limiting cases in which the ISM molecular fraction is either $\mu = 0$ (fully atomic) or $\mu = 1$ (fully molecular).

H_2 photodissociating UV radiation field. This requires high densities, and the presence of a sufficient amount of dust (see also Fig. 5). Fig. 9 shows a clear spatial segregation between regions of high and low τ_V . The former have a low volume filling factor, high dust temperatures, and dominate the FIR emission. Low- τ_V regions, previously cleared of dust and gas by stellar feedback, determine the β slope, and provide most of the UV contribution. Such two-phase configuration, made of dense, opaque clouds and semitransparent, diffuse medium, produces the observed spatial separation between UV and FIR emission.

This implies that the IRX– β values of our simulated galaxies are located above the relation predicted by models in which MCs are externally illuminated and contain relatively cold dust (Ferrara et al. 2017). Our results are in line with the suggestion by Casey et al. (2014), i.e. that galaxies with $> 50 M_\odot \text{yr}^{-1}$ are dominated at all epochs by short bursts producing young OB stars that are primarily enshrouded in thick dust cocoons. The IRX– β emerging from SERRA seems broadly consistent with most high- z observations (Laporte et al. 2017a; Fudamoto et al. 2020; Harikane et al. 2020). However, we struggle to reproduce the relation when we consider upper limits (Bouwens et al. 2016; Fujimoto et al. 2017), and some of the detections (Barisic et al. 2017). The origin of this tension is twofold.

From the observational side, it is very difficult to determine the TIR luminosity. The information is typically recovered from an SED fitting with a grey-body spectrum containing three parameters, namely (a) the dust mass (M_d), (b) the emissivity (β_d), and (c) the temperature T_{SED} . Typically, only few (one to two) continuum bands are available for most high- z targets (but see Bakx et al. 2021), so most determinations are done by assuming a T_{SED} based on low- z estimates and templates (e.g. Barisic et al. 2017; Béthermin et al. 2020, see Sommovigo et al. 2021 for alternatives). Since $L_{\text{TIR}} \propto M_d T_{\text{SED}}^{4+\beta_d}$ and typically $\beta_d \sim 1.7\text{--}2.0$, IRX is extremely sensitive to the estimated or assumed T_{SED} value. Observations (Schreiber et al. 2018; Bakx et al. 2021) and models (Sommovigo et al. 2022) indicate that T_{SED} increases towards high redshifts. Thus, the IRX value of the currently available targets might be underestimated, perhaps indicating that at least some of the galaxies in the EoR are already highly obscured (Fudamoto et al. 2021). More

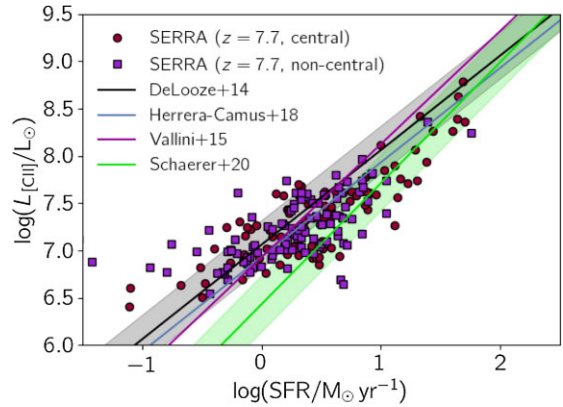


Figure 12. The integrated [C II]–SFR relation found in SERRA. Along with SERRA data at $z = 7.7$ divided into the central and non-central sample, we show the results obtained from local observations (De Looze et al. 2014; Herrera-Camus et al. 2018), the relation found at $z = 4\text{--}6$ by ALPINE (SFR $\gtrsim 10 M_\odot \text{yr}^{-1}$; Schaefer et al. 2020), and the results from physical motivated models (Vallini et al. 2015, $Z = 0.5 Z_\odot$).

robust dust temperature measurements, only made possible through high-frequency ALMA observations (e.g. BAND8/9), should relieve part of the current tension.

From the modelling side, our simulations might fall short in producing low obscuration systems, perhaps due to an insufficient feedback strength. In fact, the feedback treatment in SERRA, though accurate, is far from being complete, e.g. it lacks an explicit model for clustered SNe (Gentry et al. 2017; Martizzi 2020), and cosmic rays (Semenov, Kravtsov & Caprioli 2021; Rodríguez Montero et al. 2022), which at least locally are important contributors to the ISM energy budget. Their inclusion might change the emission properties of our galaxies.

In addition, a resolution of ~ 10 pc does not allow us to resolve the internal structure of MCs, where most of the simulated FIR is produced. The internal gas/dust distribution in an MC can dramatically affect the dust temperature, as shown by Sommovigo et al. (2020). For example, a uniform distribution might result in dust as hot as $\langle T_d \rangle_L \simeq 120$ K; when a more physical profile accounting for the effects of radiation pressure is adopted, the mean temperature drops to $\langle T_d \rangle_L \simeq 55$ K. Modelling the internal structure of MCs is beyond the reach of even the most refined cosmological zoom-in simulations.

Finally, simulations of individual MCs show that – depending on the metallicity, turbulence, and the observed band – 15 per cent to 70 per cent of the photons can escape from the cloud before it is disrupted (Decataldo et al. 2020; Kimm et al. 2022). If true, MCs would contribute significantly to UV emission, at the same time reducing the FIR emission from our galaxies. Further exploration of this aspect is ongoing.

3.6.3 Line emission properties

The (integrated) [C II]–SFR relation is presented in Fig. 12. Overall, SERRA galaxies at $z = 7.7$ are consistent with local data (De Looze et al. 2014; Herrera-Camus et al. 2018), albeit with a larger scatter. This is expected on the basis of the early work by Carniani et al. (2018a) analysing 20 targets, and of the more recent analysis of the ALPINE sample presented in Schaefer et al. (2020, 118 targets). The scatter in the relation is driven by the larger spread of physical properties (such as n , Z , κ_s) deduced for high- z galaxies (Vallini et al.

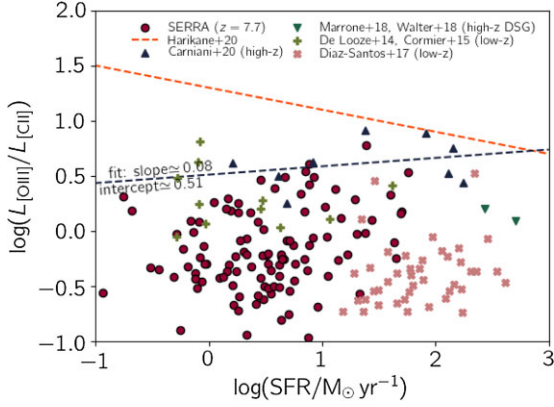


Figure 13. [O III]-to-[C II] ratio as a function of SFR. We plot the collection of observations obtained for normal high- z galaxies ($\text{SFR} < 100 \text{ M}_{\odot} \text{ yr}^{-1}$; Carniani et al. 2020) and dusty star-forming galaxies ($\text{SFR} > 100 \text{ M}_{\odot} \text{ yr}^{-1}$; Marrone et al. 2018; Walter et al. 2018), along with data for local normal (Díaz-Santos et al. 2017) and dwarf (De Looze et al. 2014; Cormier et al. 2015) galaxies. We also plot the fits from Harikane et al. (2020) and Carniani et al. (2020, computed in the present, best-fitting parameters indicated in the figure).

2015; Ferrara et al. 2019); further, the scatter appears to be larger for non-central objects, as a consequence of the interactions with their nearby more massive galaxy.

Overall, SERRA galaxies fall on to the ALPINE relation, but some tension seems present at $\text{SFR} \lesssim 1 \text{ M}_{\odot} \text{ yr}^{-1}$, where the simulated data seem to flatten and join the local De Looze et al. (2014) relation. To this concern, we note that the detection limit for ALPINE galaxies is about $\text{SFR} \gtrsim 10 \text{ M}_{\odot} \text{ yr}^{-1}$ (Le Fèvre et al. 2020; Schaerer et al. 2020). Deeper ALMA observations would be needed to probe the [C II]–SFR at more feeble star formation levels. Additionally, for SERRA galaxies at $z = 7.7$, the [C II] trend at $\text{SFR} \lesssim 1 \text{ M}_{\odot} \text{ yr}^{-1}$ shows an offset: Small central galaxies tend to have lower [C II] with respect to non-central ones with the same SFR. This is mostly due to the fact that non-central are contaminated, i.e. they are formed in an environment that is pre-enriched by their more massive companion.

While the median values of integrated [C II]–SFR present little differences at high and low redshift, recall that SERRA galaxies are typically located below the resolved $\Sigma_{\text{[C II]}}-\Sigma_{\text{SFR}}$ relation, as also found by high- z observations (Carniani et al. 2018a). Such [C II] deficiency has been discussed for a sub-sample of SERRA galaxies in Pallottini et al. (2019) and Vallini et al. (2021). It has been interpreted as a signature of an ongoing bursty star formation activity in these galaxies (high κ_s ; Ferrara et al. 2019, see Fig. 6).

Because of the increasing availability of [O III] 88 μm line observations, the [C II]/[O III] ratio has become a viable tool to study the high- z ISM. In Fig. 13, we plot the predicted ratio for the SERRA sample as a function of SFR, along with an updated collection of both high- z and local observations. The $L_{\text{[O III]}}/L_{\text{[C II]}}$ ratio for SERRA galaxies is in the range 0.1–10, and shows only a mild correlation with SFR. A non-negligible fraction of our systems has a low $L_{\text{[O III]}}/L_{\text{[C II]}}$, as a result of the intermittent star formation activity discussed in Section 3.3.1. If the SFR is quenched for more than $\simeq 20 \text{ Myr}$, the production of O^{++} ionizing photons drops, and the [O III] emission consequently fades away. This effect might be overestimated in SERRA, since in principle a better mass resolution would yield a finer sampling of the SFR process in those cases where the stellar feedback suppresses the SFR without completely quenching it. However, even simulations with a better mass resolution (e.g. Gutcke et al. 2022, $\simeq 4 \text{ M}_{\odot}$ versus

$\simeq 1.2 \times 10^4 \text{ M}_{\odot}$ adopted here) show a complete quenching of the SFR activity for long periods of time in low-mass ($M_{*} \lesssim 10^9 \text{ M}_{\odot}$) systems.

Moreover, the observed $L_{\text{[O III]}}/L_{\text{[C II]}}$ values (Harikane et al. 2020) must be down revised when accounting for the concentration bias (Carniani et al. 2020), i.e. since [C II] is more extended than [O III], its low surface brightness emission is easier to miss, and implies that $L_{\text{[C II]}}$ can be underestimated by a factor of $\simeq 2$, depending on the angular resolution and signal-to-noise ratio (S/N) of the observation.

Fitting the data from Carniani et al. (2020), we obtain

$$\log \frac{L_{\text{[O III]}}}{L_{\text{[C II]}}} = (0.08 \pm 0.01) \log \frac{\text{SFR}}{\text{M}_{\odot} \text{ yr}^{-1}} + 0.51 \pm 0.02 \quad (13)$$

i.e. a flatter curve with respect to Harikane et al. (2020), with ratios that are about one order of magnitude lower at $\text{SFR} \sim 1 \text{ M}_{\odot} \text{ yr}^{-1}$, where we currently have very few detections. Indeed, some of our galaxies can match the observed ratios; however, the bulk of SERRA galaxies have $L_{\text{[O III]}}/L_{\text{[C II]}}$ that are lower than the observed ones. It is interesting to note that while Dianthus (Fig. 8) and Zinnia (Fig. 9) have very similar properties (M_{*} , SFR, κ_s , ...), $L_{\text{[O III]}}/L_{\text{[C II]}}$ is $\simeq 0.2$ and $\simeq 5.0$, respectively; the former galaxy is a disc, the latter is a merger, which hints at the possibility that the dynamical state of the system can play an important role in the ratio determination; we are planning to explore the aspect more systematically in the future (see Rizzo et al. 2022).

While we need more observations to robustly determine a relation at high z , this is an indication that the ratios for high- z targets tend to be more in line with those obtained for local galaxies (De Looze et al. 2014; Cormier et al. 2015; Díaz-Santos et al. 2017), and the SERRA ones (see also Vallini et al. 2021). Thus, we find no need to invoke alternative explanations, such as a top-heavy IMF or differential enrichment patterns for C and O, as explored in Arata et al. (2020) and Katz et al. (2022), which adopt the unrevised values for the ratio. While we can expect that variations of C and O abundances are present in the ISM of high- z galaxies – which also have other implications and should be explored – the current data do not seem to call for extreme scenarios strongly. We stress that the above discussion must be taken with a grain of salt, as currently only 11 targets at high z have both [C II] and [O III] detections; in particular, it is still unclear if we are picking the brightest, more concentrated, [O III] emitter or seeing the bulk of the population. Considering that observational evidence and models agree on a very mild evolution of $L_{\text{[C II]}}-\text{SFR}$ with z , the latter option would imply that an evolution of the $L_{\text{[O III]}}-\text{SFR}$ that is larger than predicted by the simulations, which would entail a revision of part of our modelling: Only future observations will be able to test the different scenarios.

To conclude, we analyse the SFR dependence of different lines ([C II], [O III], and [O I] 63 μm) for simulated galaxies and compare it with all the available low-redshift data to assess whether early systems differ substantially from their local counterparts in this respect. In Fig. 14, we show the results using a collection of diverse samples, i.e. starbursts, dwarfs, $z \sim 0.5$, and ULIRGs (De Looze et al. 2014).

Regarding the [C II], the bulk of SERRA follows the starbursts and $z \lesssim 0.5$ relation; interestingly, at $\text{SFR} \gtrsim 3 \text{ M}_{\odot} \text{ yr}^{-1}$, the simulated galaxies are intermediate between starbursts and ULIRGs, and far from the slope characterizing the dwarf galaxy population. Qualitatively, this is expected considering that SERRA galaxies have high IRX values for their β (Fig. 11), a feature shared by many high- z observed targets. Also, some of the REBELS galaxies appear as scaled-down versions of dusty star-forming galaxies (Fudamoto et al. 2021).

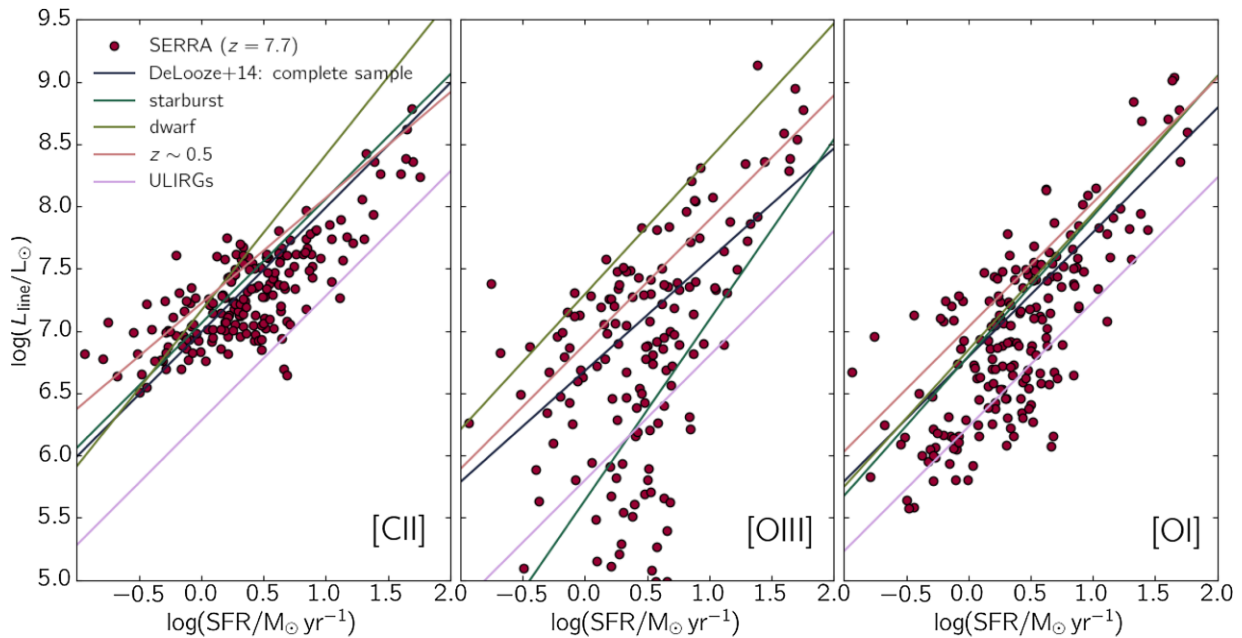


Figure 14. SERRA emission line predictions compared to available local data. We show [C II], [O III], and [O I] as a function of SFR in the left-hand, central, and right-hand panel, respectively. Fits to observed trends for different classes of galaxies in the low- z Universe are shown. The dwarf galaxy observations are taken from De Looze et al. (2014), as well as the classification and the relative fits, which are based on additional data from Brauher, Dale & Helou (2008), Graciá-Carpio et al. (2011), Sargsyan et al. (2012), Parkin et al. (2013), Díaz-Santos et al. (2013), and Farrah et al. (2013).

The [O III]–SFR relation is more complex. Most of the simulated high- z galaxies follow the same trend of $z \lesssim 0.5$ systems. However, a consistent fraction of the sample is found along the starburst locus; the remaining part contains galaxies that have their SFR temporarily quenched, and therefore showing a strongly reduced [O III] luminosity. The presence of a single trend for [C II] and two trends for [O III] is the reason why no $L_{[\text{OIII}]} / L_{[\text{CII}]}$ –SFR relation can be identified (see Fig. 13). The quenching is not fully captured by the value of the sSFR: Also the burstiness κ_s plays a role, along with mean gas density and metallicity, which can give secondary dependences on the [O III] line (Vallini et al. 2021). The situation is complex, also considering that consistency with local line luminosity–SFR scaling relations (Fig. 14) does not automatically imply consistency of the line ratio versus SFR scaling (Fig. 13); we aim at addressing this point in a following work.

Finally, [O I] is an important tracer of the dense atomic and molecular regions, but so far it has been detected only in a single $z \simeq 6$ lensed galaxy with APEX (Rybak et al. 2020). Similarly to [C II], [O I] predictions from SERRA galaxies follow the trend for starbursts and $z \lesssim 0.5$ targets, even though the scatter appears somewhat larger. Although [O I] 63 μm is more luminous than [C II], unfortunately it falls in ALMA BAND9 for a $z \simeq 6$ object. Let us focus on an SFR $\simeq 50 M_\odot \text{yr}^{-1}$ galaxy with a full width at half-maximum of $\simeq 200 \text{ km s}^{-1}$ (Kohandel et al. 2019). Such object has $L_{\text{O}63\mu\text{m}} \simeq 5 \times 10^8 L_\odot$; thus, detection ($S/N = 5$) in BAND9 would require $\simeq 6$ h of observing time.²⁶

Note that [O I] 145 μm is shifted in the more favourable ALMA BAND7; the trend with SFR of the luminosity of [O I] 145 μm is similar to [O I] 63 μm (see also Lupi et al. 2020). However, [O I] 145 μm is usually ~ 10 times fainter; thus, a detection

would require $\simeq 7$ h of observing time, i.e. similar to the other line.

Albeit challenging, detecting [O I] is feasible and crucial to clarify, for example, whether a differential C/O enrichment is in place at high z . While such an experiment can be attempted by using [C II] and [O III] (Arata et al. 2020; Harikane et al. 2020), the latter is strongly dependent on ionizing radiation; thus, [O I] would represent an independent and cleaner probe. Further, [O I] lines fall both in BAND7 and BAND9; while trying to use the latter is typically regarded as a risky strategy, observations in BAND9 could simultaneously give both the [O I] and crucial information to constrain the dust temperature (Bakx et al. 2020), as it is closer to the continuum peak.

4 SUMMARY

We introduce SERRA, a suite of zoom-in high-resolution ($1.2 \times 10^4 M_\odot$, $\simeq 25$ pc at $z = 7.7$) cosmological simulations including non-equilibrium chemistry and on-the-fly radiative transfer. The outputs are post-processed to derive galaxy UV + FIR continuum and emission line properties. Results are compared with available multiwavelength data to constrain the physical properties (e.g. SFRs, stellar/gas/dust mass, metallicity) of high-redshift $6 \lesssim z \lesssim 15$ galaxies.

In this flagship paper, we have focused our attention on the $z = 7.7$ sample, consisting of 202 targets with a stellar mass range $10^7 M_\odot \lesssim M_\star \lesssim 5 \times 10^{10} M_\odot$. These objects are resolved with a mass (spatial) resolution of $1.2 \times 10^4 M_\odot$ ($\simeq 25$ pc). The main highlights are the following.

- (i) All SERRA galaxies show a time-increasing SFR featuring rapid fluctuations, particularly evident at low masses, caused by stellar feedback and merging episodes. The sSFR ranges from sSFR $\sim 100 \text{ Gyr}^{-1}$ for young ($t_\star \lesssim 100 \text{ Myr}$), small galaxies ($M_\star \lesssim 10^8 M_\odot$) to sSFR $\sim 10 \text{ Gyr}^{-1}$ for older ($t_\star \gtrsim 200 \text{ Myr}$) more massive ones

²⁶This estimate is critically dependent on the galaxy location with respect to the atmospheric absorption lines, which are abundant in BAND9.

($M_* \gtrsim 10^9 M_\odot$), in good agreement with high- z data (Jiang et al. 2013; Rinaldi et al. 2021).

(ii) The simulated stellar-to-halo mass relation is consistent with abundance matching works (Behroozi et al. 2013a) for large halo masses, i.e. $M_h \gtrsim 5 \times 10^{10} M_\odot$. In smaller haloes ($M_h \sim 10^9 M_\odot$), the intense radiation from the first few formation events easily dissociates H_2 , causing relatively extended periods during which star formation is completely quenched, and the galaxy stays well below the Behroozi et al. (2013a) relation. After a series of bursts, a sufficient amount of dust is produced to allow an efficient self-shielding of H_2 , and a continuous star formation activity, which eventually brings the galaxy on to the stellar-to-halo mass relation.

(iii) On average, SERRA galaxies are ‘bursty’, i.e. they are located above the Schmidt–Kennicutt relation, with a burstiness parameter (equation 10) $\kappa_s = 3.03_{-1.8}^{+4.9}$. For galaxies with $\Sigma_{\text{SFR}} \gtrsim 10 M_\odot \text{ yr}^{-1} \text{ kpc}^{-2}$, κ_s is higher and in agreement with Vallini et al. (2021), who infer $\kappa_s \simeq 36.3$ for 11 observed high- z galaxies.

(iv) The size–stellar mass relation from SERRA is $\log(r_{\text{UV}}/\text{kpc}) \simeq 0.25 \log(M_*/M_\odot) - 3.1$ (see equation 11). The relation has the same slope as the one observed in the local Universe (Brodie et al. 2011; Norris et al. 2014), but it is downshifted by about one order of magnitude because of redshift evolution (cf. Shibuya et al. 2015). The data from SERRA are consistent with lensed galaxies observed at high z (Bouwens et al. 2017; Vanzella et al. 2019), but our median has a systematic offset of a factor of $\simeq 2$.

(v) The bulk of SERRA galaxies have $-2.5 < \beta < -1$, as expected from a stellar population dominated by relatively unobscured, young stars. However, their IRX is typically ~ 10 , as expected from evolved and obscured systems. The origin of this apparent contradiction resides in the multiphase ISM structure in these systems, consisting of IR-emitting molecular clumps embedded in a semitransparent, UV-emitting diffuse component. This configuration also produces a UV versus dust continuum spatial offset.

(vi) Regarding line emission, SERRA is consistent with the [C II]–SFR observed at high z (Schaefer et al. 2020) and with the bulk of the inferred $L_{[\text{O III}]}/L_{[\text{C II}]}$, when the observational concentration bias is accounted for (Carniani et al. 2020). Further, our results suggest that the dynamical state of the system (merger versus disc) can play an important role in determining the $L_{[\text{O III}]}/L_{[\text{C II}]}$ ratio.

(vii) Detection of [O I] is feasible but challenging, i.e. for an $\text{SFR} \simeq 50 M_\odot \text{ yr}^{-1}$ galaxy, about $\simeq 6(7)$ h in ALMA BAND9 (BAND7) are needed for the $63 \mu\text{m}$ ($145 \mu\text{m}$) line. Its detection will bring crucial information on the metal enrichment patterns of individual elements in early galaxy systems. While risky, observations in BAND9 would be particularly rewarding, as they could simultaneously give both the [O I] and crucial information to constrain the dust temperature, as it is closer to the continuum peak.

ACKNOWLEDGEMENTS

AP, AF, MK, SC, LV, and LS acknowledge support from the ERC Advanced Grant INTERSTELLAR H2020/740120 (PI: Ferrara). SS acknowledges support from the ERC Starting Grant NEFERTITI H2020/804240 (PI: Salvadori). Any dissemination of results must indicate that it reflects only the author’s view and that the Commission is not responsible for any use that may be made of the information it contains. This research was supported by the Munich Institute for Astro- and Particle Physics (MIAPP) of the DFG cluster of excellence ‘Origin and Structure of the Universe’. Partial support from the Carl Friedrich von Siemens-Forschungspreis der Alexander von Humboldt-Stiftung Research Award is kindly acknowledged. We acknowledge the CINECA award under the ISCRA initiative, for the MNRAS 513, 5621–5641 (2022)

availability of high performance computing resources and support from the Class B project SERRA HP10BPUZ8F (PI: Pallottini). We gratefully acknowledge computational resources of the Center for High Performance Computing (CHPC) at SNS. We acknowledge usage of the PYTHON programming language (Van Rossum & de Boer 1991; Van Rossum & Drake 2009), ASTROPY (Astropy Collaboration et al. 2013), CYTHON (Behnel et al. 2011), MATPLOTLIB (Hunter 2007), NUMPY (van der Walt, Colbert & Varoquaux 2011), PYNBODY (Pontzen et al. 2013), and SCIPY (Virtanen et al. 2020).

DATA AVAILABILITY

The derived data generated in this research will be shared on reasonable requests to the corresponding author. Part of the data used for this study is available at the website http://cosmology.sns.it/data_access.html.

REFERENCES

- Agertz O., Kravtsov A. V., 2015, *ApJ*, 804, 18
 Agertz O., Kravtsov A. V., Leitner S. N., Gnedin N. Y., 2013, *ApJ*, 770, 25
 Arata S., Yajima H., Nagamine K., Abe M., Khochfar S., 2020, *MNRAS*, 498, 5541
 Asplund M., Grevesse N., Sauval A. J., Scott P., 2009, *ARA&A*, 47, 481
 Astropy Collaboration et al., 2013, *A&A*, 558, A33
 Aubert D., Teyssier R., 2008, *MNRAS*, 387, 295
 Baes M., Camps P., 2015, *Astron. Comput.*, 12, 33
 Bakx T. J. L. C. et al., 2020, *MNRAS*, 493, 4294
 Bakx T. J. L. C. et al., 2021, *MNRAS*, 508, L58
 Barisic I. et al., 2017, *ApJ*, 845, 41
 Behnel S., Bradshaw R., Citro C., Dalcin L., Seljebotn D., Smith K., 2011, *Comput. Sci. Eng.*, 13, 31
 Behrens C., Pallottini A., Ferrara A., Gallerani S., Vallini L., 2018, *MNRAS*, 477, 552
 Behrens C., Pallottini A., Ferrara A., Gallerani S., Vallini L., 2019, *MNRAS*, 486, 2197
 Behroozi P. S., Silk J., 2015, *ApJ*, 799, 32
 Behroozi P. S., Wechsler R. H., Wu H.-Y., 2013a, *ApJ*, 762, 109
 Behroozi P. S., Wechsler R. H., Wu H.-Y., Busha M. T., Klypin A. A., Primack J. R., 2013b, *ApJ*, 763, 18
 Behroozi P. S., Wechsler R. H., Conroy C., 2013c, *ApJ*, 770, 57
 Behroozi P., Wechsler R. H., Hearin A. P., Conroy C., 2019, *MNRAS*, 488, 3143
 Bertelli G., Bressan A., Chiosi C., Fagotto F., Nasi E., 1994, *A&AS*, 106, 275
 Béthermin M. et al., 2020, *A&A*, 643, A2
 Bothwell M. S. et al., 2010, *MNRAS*, 405, 219
 Bouché N. et al., 2007, *ApJ*, 671, 303
 Bouwens R. J. et al., 2015, *ApJ*, 803, 34
 Bouwens R. J. et al., 2016, *ApJ*, 833, 72
 Bouwens R. J., Illingworth G. D., Oesch P. A., Maseda M., Ribeiro B., Stefanon M., Lam D., 2017, preprint ([arXiv:1711.02090](https://arxiv.org/abs/1711.02090))
 Bouwens R. J. et al., 2021, preprint ([arXiv:2106.13719](https://arxiv.org/abs/2106.13719))
 Bovino S., Grassi T., Capelo P. R., Schleicher D. R. G., Banerjee R., 2016, *A&A*, 590, A15
 Bradac M. et al., 2017, *ApJ*, 836, L2
 Brauer J. R., Dale D. A., Helou G., 2008, *ApJS*, 178, 280
 Brodie J. P., Romanowsky A. J., Strader J., Forbes D. A., 2011, *AJ*, 142, 199
 Bruzual G., Charlot S., 2003, *MNRAS*, 344, 1000
 Calzetti D., Kinney A. L., Storchi-Bergmann T., 1994, *ApJ*, 429, 582
 Camps P., Baes M., 2015, *Astron. Comput.*, 9, 20
 Capak P. L. et al., 2015, *Nature*, 522, 455
 Capelo P. R., Bovino S., Lupi A., Schleicher D. R. G., Grassi T., 2018, *MNRAS*, 475, 3283
 Carniani S. et al., 2017, *A&A*, 605, A42
 Carniani S. et al., 2018a, *MNRAS*, 478, 1170
 Carniani S., Maiolino R., Smit R., Amorin R., 2018b, *ApJ*, 854, L7
 Carniani S. et al., 2020, *MNRAS*, 499, 5136

- Casey C. M. et al., 2014, *ApJ*, 796, 95
- Ceverino D., Primack J., Dekel A., 2015, *MNRAS*, 453, 408
- Ceverino D., Glover S. C. O., Klessen R. S., 2017, *MNRAS*, 470, 2791
- Chabrier G., 2003, *PASP*, 115, 763
- Chardin J., Kulkarni G., Haehnelt M. G., 2018, *MNRAS*, 478, 1065
- Cooray A., Origins Space Telescope STDT, Study Team, 2020, American Astronomical Society Meeting Abstracts #235. p. 311.02
- Cormier D. et al., 2015, *A&A*, 578, A53
- Correa C. A., Wyithe J. S. B., Schaye J., Duffy A. R., 2015, *MNRAS*, 450, 1514
- Courant R., Friedrichs K., Lewy H., 1928, *Math. Ann.*, 100, 32
- Curti M., Cresci G., Mannucci F., Marconi A., Maiolino R., Esposito S., 2017, *MNRAS*, 465, 1384
- D'Odorico V. et al., 2018, *ApJ*, 863, L29
- Daddi E. et al., 2010, *ApJ*, 713, 686
- Dayal P., Ferrara A., 2018, *Phys. Rep.*, 780, 1
- De Looze I. et al., 2014, *A&A*, 568, A62
- De Looze I. et al., 2020, *MNRAS*, 496, 3668
- Decataldo D., Pallottini A., Ferrara A., Vallini L., Gallerani S., 2019, *MNRAS*, 487, 3377
- Decataldo D., Lupi A., Ferrara A., Pallottini A., Fumagalli M., 2020, *MNRAS*, 497, 4718
- Deparis N., Aubert D., Ocvirk P., Chardin J., Lewis J., 2019, *A&A*, 622, A142
- Di Mascia F. et al., 2021, *MNRAS*, 503, 2349
- Díaz-Santos T. et al., 2013, *ApJ*, 774, 68
- Díaz-Santos T. et al., 2017, *ApJ*, 846, 32
- Dubois Y., Commerçon B., 2016, *A&A*, 585, A138
- Dubois Y., Teyssier R., 2008, *A&A*, 477, 79
- Dunlop J. S., 2013, in Wiklind T., Mobasher B., Bromm V., eds, *Astrophysics and Space Science Library*, Vol. 396, *The First Galaxies*. Springer-Verlag, Berlin, p. 223
- Egami E. et al., 2018, *PASA*, 35, 48
- Eisenstein D. J., Hu W., 1998, *ApJ*, 496, 605
- Emerick A., Bryan G. L., Mac Low M.-M., 2019, *MNRAS*, 482, 1304
- Engels J. F., Schmidt W., Niemeyer J., 2019, *MNRAS*, 482, 4654
- Faisst A. L., Fudamoto Y., Oesch P. A., Scoville N., Riechers D. A., Pavesi R., Capak P., 2020, *MNRAS*, 498, 4192
- Fakhouri O., Ma C.-P., Boylan-Kolchin M., 2010, *MNRAS*, 406, 2267
- Farcy M., Rosdahl J., Dubois Y., Blaizot J., Martin-Alvarez S., 2022, preprint (arXiv:2202.01245)
- Farrar D. et al., 2013, *ApJ*, 776, 38
- Federrath C., Klessen R. S., 2013, *ApJ*, 763, 51
- Feng Y., Di-Matteo T., Croft R. A., Bird S., Battaglia N., Wilkins S., 2016, *MNRAS*, 455, 2778
- Ferland G. J. et al., 2013, *Rev. Mex. Astron. Astrofis.*, 49, 137
- Ferland G. J. et al., 2017, *Rev. Mex. Astron. Astrofis.*, 53, 385
- Ferrara A., Hirashita H., Ouchi M., Fujimoto S., 2017, *MNRAS*, 471, 5018
- Ferrara A., Vallini L., Pallottini A., Gallerani S., Carniani S., Kohandel M., Decataldo D., Behrens C., 2019, *MNRAS*, 489, 1
- Ferrara A. et al., 2022, *MNRAS*, 512, 58
- Feruglio C. et al., 2018, *A&A*, 619, A39
- Fiacconi D., Feldmann R., Mayer L., 2015, *MNRAS*, 446, 1957
- Fudamoto Y. et al., 2020, *A&A*, 643, A4
- Fudamoto Y. et al., 2021, *Nature*, 597, 489
- Fujimoto S., Ouchi M., Shibuya T., Nagai H., 2017, *ApJ*, 850, 83
- Fujimoto S. et al., 2019, *ApJ*, 887, 107
- Fujimoto S. et al., 2020, *ApJ*, 900, 1
- Gallerani S., Ferrara A., Neri R., Maiolino R., 2014, *MNRAS*, 445, 2848
- Gallerani S., Pallottini A., Feruglio C., Ferrara A., Maiolino R., Vallini L., Riechers D. A., Pavesi R., 2018, *MNRAS*, 473, 1909
- Galli D., Palla F., 1998, *A&A*, 335, 403
- Gelli V., Salvadori S., Pallottini A., Ferrara A., 2020, *MNRAS*, 498, 4134
- Gelli V., Salvadori S., Ferrara A., Pallottini A., Carniani S., 2021, *ApJ*, 913, L25
- Gentry E. S., Krumholz M. R., Dekel A., Madau P., 2017, *MNRAS*, 465, 2471
- Ginolfi M. et al., 2020, *A&A*, 633, A90
- Gnedin N. Y., 2010, *ApJ*, 721, L79
- Gnedin N. Y., 2014, *ApJ*, 793, 29
- Gnedin N. Y., 2016, *ApJ*, 833, 66
- Gnedin N. Y., Abel T., 2001, *New Astron.*, 6, 437
- Gnedin N. Y., Hollon N., 2012, *ApJS*, 202, 13
- González V., Labbé I., Bouwens R. J., Illingworth G., Franx M., Kriek M., Brammer G. B., 2010, *ApJ*, 713, 115
- Graciá-Carpio J. et al., 2011, *ApJ*, 728, L7
- Grassi T., Bovino S., Schleicher D. R. G., Prieto J., Seifried D., Simoncini E., Gianturco F. A., 2014, *MNRAS*, 439, 2386
- Guillet T., Teyssier R., 2011, *J. Comput. Phys.*, 230, 4756
- Gutcke T. A., Pakmor R., Naab T., Springel V., 2022, *MNRAS*, 513, 1372
- Haardt F., Madau P., 2012, *ApJ*, 746, 125
- Habing H. J., 1968, *Bull. Astron. Inst. Neth.*, 19, 421
- Hahn O., Abel T., 2011, *MNRAS*, 415, 2101
- Harikane Y. et al., 2018, *ApJ*, 859, 84
- Harikane Y. et al., 2020, *ApJ*, 896, 93
- Hashimoto T. et al., 2019, *PASJ*, 71, 71
- Heiderman A., Evans Neal J. I., Allen L. E., Huard T., Heyer M., 2010, *ApJ*, 723, 1019
- Herrera-Camus R. et al., 2015, *ApJ*, 800, 1
- Herrera-Camus R. et al., 2018, *ApJ*, 861, 95
- Hindmarsh A. C., 2019, *Astrophysics Source Code Library*, record ascl:1905.021
- Hirashita H., Ferrara A., 2002, *MNRAS*, 337, 921
- Hopkins P. F., Kereš D., Oñorbe J., Faucher-Giguère C.-A., Quataert E., Murray N., Bullock J. S., 2014, *MNRAS*, 445, 581
- Hopkins P. F. et al., 2018, *MNRAS*, 480, 800
- Hopkins P. F., Grudić M. Y., Wetzel A., Kereš D., Faucher-Giguère C.-A., Ma X., Murray N., Butcher N., 2020, *MNRAS*, 491, 3702
- Hunter J. D., 2007, *Comput. Sci. Eng.*, 9, 90
- Iapichino L., Federrath C., Klessen R. S., 2017, *MNRAS*, 469, 3641
- Inoue A. K. et al., 2016a, *Science*, 352, 1559
- Inoue S., Dekel A., Mandelker N., Ceverino D., Bournaud F., Primack J., 2016b, *MNRAS*, 456, 2052
- Ivlev A. V., Padovani M., Galli D., Caselli P., 2015, *ApJ*, 812, 135
- Jaacks J., Thompson R., Finkelstein S. L., Bromm V., 2018, *MNRAS*, 475, 4396
- Jiang L. et al., 2013, *ApJ*, 773, 153
- Johnson J. L., Dalla V. C., Khochfar S., 2013, *MNRAS*, 428, 1857
- Jones G. C., Willott C. J., Carilli C. L., Ferrara A., Wang R., Wagg J., 2017, *ApJ*, 845, 175
- Jura M., 1975, *ApJ*, 197, 575
- Kanekar N., Wagg J., Ram Chary R., Carilli C. L., 2013, *ApJ*, 771, L20
- Kannan R., Garaldi E., Smith A., Pakmor R., Springel V., Vogelsberger M., Hernquist L., 2022, *MNRAS*, 511, 4005
- Katz H., Kimm T., Sijacki D., Haehnelt M. G., 2017, *MNRAS*, 468, 4831
- Katz H., Laporte N., Ellis R. S., Devriendt J., Slyz A., 2019, *MNRAS*, 484, 4054
- Katz H. et al., 2022, *MNRAS*, 510, 5603
- Kennicutt R. C., Jr, 1998, *ApJ*, 498, 541
- Kennicutt R. C., Evans N. J., 2012, *ARA&A*, 50, 531
- Kewley L. J., Dopita M. A., 2002, *ApJS*, 142, 35
- Kimm T., Bieri R., Geen S., Rosdahl J., Blaizot J., Michel-Dansac L., Garel T., 2022, *ApJS*, 259, 21
- Knebe A. et al., 2013, *MNRAS*, 428, 2039
- Knudsen K. K., Richard J., Kneib J.-P., Jauzac M., Clément B., Drouart G., Egami E., Lindroos L., 2016, *MNRAS*, 462, L6
- Kohandel M., Pallottini A., Ferrara A., Zanella A., Behrens C., Carniani S., Gallerani S., Vallini L., 2019, *MNRAS*, 487, 3007
- Kohandel M., Pallottini A., Ferrara A., Carniani S., Gallerani S., Vallini L., Zanella A., Behrens C., 2020, *MNRAS*, 499, 1250
- Kroupa P., 2001, *MNRAS*, 322, 231
- Krumholz M. R., 2015, preprint (arXiv:1511.03457)
- Laporte N. et al., 2017a, *ApJ*, 837, L21
- Laporte N., Nakajima K., Ellis R. S., Zitrin A., Stark D. P., Mainali R., Roberts-Borsani G. W., 2017b, *ApJ*, 851, 40

- Le Fèvre O. et al., 2020, *A&A*, 643, A1
- Leitherer C. et al., 1999, *ApJS*, 123, 3
- Leung T. K. D., Pallottini A., Ferrara A., Mac Low M.-M., 2020, *ApJ*, 895, 24
- Liang L. et al., 2019, *MNRAS*, 489, 2072
- Loiacono F. et al., 2021, *A&A*, 646, A76
- Lovell C. C., Vijayan A. P., Thomas P. A., Wilkins S. M., Barnes D. J., Irodotou D., Roper W., 2021, *MNRAS*, 500, 2127
- Lupi A., 2019, *MNRAS*, 484, 1687
- Lupi A., Bovino S., Capelo P. R., Volonteri M., Silk J., 2018, *MNRAS*, 474, 2884
- Lupi A., Pallottini A., Ferrara A., Bovino S., Carniani S., Vallini L., 2020, *MNRAS*, 496, 5160
- Ma X. et al., 2018, *MNRAS*, 478, 1694
- Mac Low M.-M., 1999, *ApJ*, 524, 169
- Madau P., Dickinson M., 2014, *ARA&A*, 52, 415
- Maio U., Tescari E., 2015, *MNRAS*, 453, 3798
- Maiolino R., Mannucci F., 2019, *A&AR*, 27, 3
- Maiolino R. et al., 2015, *MNRAS*, 452, 54
- Mancini M., Schneider R., Graziani L., Valiante R., Dayal P., Maio U., Ciardi B., Hunt L. K., 2015, *MNRAS*, 451, L70
- Marrone D. P. et al., 2018, *Nature*, 553, 51
- Martizzi D., 2020, *MNRAS*, 492, 79
- Matthee J. et al., 2017, *ApJ*, 851, 145
- Meurer G. R., Heckman T. M., Leitherer C., Kinney A., Robert C., Garnett D. R., 1995, *AJ*, 110, 2665
- Moster B. P., Naab T., White S. D. M., 2013, *MNRAS*, 428, 3121
- Moster B. P., Naab T., White S. D. M., 2018, *MNRAS*, 477, 1822
- Murray N., 2011, *ApJ*, 729, 133
- Murray S. G., Power C., Robotham A. S. G., 2013, *Astron. Comput.*, 3, 23
- Norris M. A. et al., 2014, *MNRAS*, 443, 1151
- O'Shea B. W., Wise J. H., Xu H., Norman M. L., 2015, *ApJ*, 807, L12
- Ocvirk P. et al., 2020, *MNRAS*, 496, 4087
- Oesch P. A., Bouwens R. J., Illingworth G. D., Labbé I., Stefanon M., 2018, *ApJ*, 855, 105
- Olsen K. P., Greve T. R., Narayanan D., Thompson R., Toft S., Brinch C., 2015, *ApJ*, 814, 76
- Olsen K., Greve T. R., Narayanan D., Thompson R., Davé R., Niebla Rios L., Stawinski S., 2017, *ApJ*, 846, 105
- Olsen K. et al., 2018, *Galaxies*, 6, 100
- Onorbe J., Garrison-Kimmel S., Maller A. H., Bullock J. S., Rocha M., Hahn O., 2014, *MNRAS*, 437, 1894
- Ostriker J. P., McKee C. F., 1988, *Rev. Mod. Phys.*, 60, 1
- Ota K. et al., 2014, *ApJ*, 792, 34
- Ouchi M. et al., 2013, *ApJ*, 778, 102
- Padovani M., Galli D., Ivlev A. V., Caselli P., Ferrara A., 2018, *A&A*, 619, A144
- Pallottini A., Ferrara A., Gallerani S., Salvadori S., D'Odorico V., 2014, *MNRAS*, 440, 2498
- Pallottini A., Ferrara A., Gallerani S., Vallini L., Maiolino R., Salvadori S., 2017a, *MNRAS*, 465, 2540
- Pallottini A., Ferrara A., Bovino S., Vallini L., Gallerani S., Maiolino R., Salvadori S., 2017b, *MNRAS*, 471, 4128
- Pallottini A. et al., 2019, *MNRAS*, 487, 1689
- Parkin T. J. et al., 2013, *ApJ*, 776, 65
- Pavesi R., Riechers D. A., Faisst A. L., Stacey G. J., Capak P. L., 2019, *ApJ*, 882, 168
- Pentericci L. et al., 2016, *ApJ*, 829, L11
- Pfommer C., Pakmor R., Schaal K., Simpson C. M., Springel V., 2017, *MNRAS*, 465, 4500
- Pillepich A. et al., 2018, *MNRAS*, 473, 4077
- Pillepich A. et al., 2019, *MNRAS*, 490, 3196
- Pizzati E., Ferrara A., Pallottini A., Gallerani S., Vallini L., Decataldo D., Fujimoto S., 2020, *MNRAS*, 495, 160
- Planck Collaboration et al., 2014, *A&A*, 571, A16
- Pontzen A., Røsvik R., Stinson G. S., Woods R., Reed D. M., Coles J., Quinn T. R., 2013, *Astrophysics Source Code Library*, record ascl:1305.002
- Popping G., Somerville R. S., Galametz M., 2017, *MNRAS*, 471, 3152
- Popping G., Narayanan D., Somerville R. S., Faisst A. L., Krumholz M. R., 2019, *MNRAS*, 482, 4906
- Rahmati A., Pawlik A. H., Raicevic M., Schaye J., 2013, *MNRAS*, 430, 2427
- Rasera Y., Teyssier R., 2006, *A&A*, 445, 1
- Richings A. J., Schaye J., Oppenheimer B. D., 2014, *MNRAS*, 442, 2780
- Rinaldi P., Caputi K. I., van Mierlo S., Ashby M. L. N., Caminha G. B., Iani E., 2021, preprint ([arXiv:2112.03935](https://arxiv.org/abs/2112.03935))
- Rizzo F., Kohandel M., Pallottini A., Zanella A., Ferrara A., Vallini L., Toft S., 2022, preprint ([arXiv:2204.05325](https://arxiv.org/abs/2204.05325))
- Rodríguez Montero F., Martín-Alvarez S., Sijacki D., Slyz A., Devriendt J., Dubois Y., 2022, *MNRAS*, 511, 1247
- Rosdahl J., Teyssier R., 2015, *MNRAS*, 449, 4380
- Rosdahl J., Blaizot J., Aubert D., Stranex T., Teyssier R., 2013, *MNRAS*, 436, 2188
- Rosdahl J., Schaye J., Dubois Y., Kimm T., Teyssier R., 2017, *MNRAS*, 466, 11
- Rosdahl J. et al., 2018, *MNRAS*, 479, 994
- Rybak M., Zavala J. A., Hodge J. A., Casey C. M., Werf P. v. d., 2020, *ApJ*, 889, L11
- Salpeter E. E., 1955, *ApJ*, 121, 161
- Sargsyan L. et al., 2012, *ApJ*, 755, 171
- Scannapieco E., Brügger M., 2010, *MNRAS*, 405, 1634
- Schaerer D., Boone F., Zamojski M., Staguhn J., Dessauges-Zavadsky M., Finkelstein S., Combes F., 2015, *A&A*, 574, A19
- Schaerer D. et al., 2020, *A&A*, 643, A3
- Schaller M., Dalla Vecchia C., Schaye J., Bower R. G., Theuns T., Crain R. A., Furlong M., McCarthy I. G., 2015, *MNRAS*, 454, 2277
- Schmidt M., 1959, *ApJ*, 129, 243
- Schreiber C., Elbaz D., Pannella M., Ciesla L., Wang T., Franco M., 2018, *A&A*, 609, A30
- Semenov V. A., Kravtsov A. V., Gnedin N. Y., 2016, *ApJ*, 826, 200
- Semenov V. A., Kravtsov A. V., Gnedin N. Y., 2018, *ApJ*, 861, 4
- Semenov V. A., Kravtsov A. V., Caprioli D., 2021, *ApJ*, 910, 126
- Sheth R. K., Tormen G., 1999, *MNRAS*, 308, 119
- Shibuya T., Ouchi M., Harikane Y., 2015, *ApJS*, 219, 15
- Smit R. et al., 2018, *Nature*, 553, 178
- Smith B. D., Regan J. A., Downes T. P., Norman M. L., O'Shea B. W., Wise J. H., 2018, *MNRAS*, 480, 3762
- Sommovigo L., Ferrara A., Pallottini A., Carniani S., Gallerani S., Decataldo D., 2020, *MNRAS*, 497, 956
- Sommovigo L., Ferrara A., Carniani S., Zanella A., Pallottini A., Gallerani S., Vallini L., 2021, *MNRAS*, 503, 4878
- Sommovigo L. et al., 2022, *MNRAS*
- Spinoglio L. et al., 2017, *PASA*, 34, e057
- Srisawat C. et al., 2013, *MNRAS*, 436, 150
- Stacey G. J., Geis N., Genzel R., Lugten J. B., Poglitsch A., Sternberg A., Townes C. H., 1991, *ApJ*, 373, 423
- Stark D. P., Schenker M. A., Ellis R., Robertson B., McLure R., Dunlop J., 2013, *ApJ*, 763, 129
- Stecher T. P., Williams D. A., 1967, *ApJ*, 149, L29
- Tacchella S., Bose S., Conroy C., Eisenstein D. J., Johnson B. D., 2018, *ApJ*, 868, 92
- Tacconi L. J. et al., 2010, *Nature*, 463, 781
- Tamura Y. et al., 2019, *ApJ*, 874, 27
- Teyssier R., 2002, *A&A*, 385, 337
- Teyssier R., Pontzen A., Dubois Y., Read J. I., 2013, *MNRAS*, 429, 3068
- Trebtsch M., Blaizot J., Rosdahl J., Devriendt J., Slyz A., 2017, *MNRAS*, 470, 224
- Ucci G. et al., 2019, *MNRAS*, 483, 1295
- Valle G., Ferrini F., Galli D., Shore S. N., 2002, *ApJ*, 566, 252
- Vallini L., Gallerani S., Ferrara A., Baek S., 2013, *MNRAS*, 433, 1567
- Vallini L., Gallerani S., Ferrara A., Pallottini A., Yue B., 2015, *ApJ*, 813, 36
- Vallini L., Ferrara A., Pallottini A., Gallerani S., 2017, *MNRAS*, 467, 1300
- Vallini L., Pallottini A., Ferrara A., Gallerani S., Sobacchi E., Behrens C., 2018, *MNRAS*, 473, 271

- Vallini L., Tielens A. G. G. M., Pallottini A., Gallerani S., Gruppioni C., Carniani S., Pozzi F., Talia M., 2019, *MNRAS*, 490, 4502
- Vallini L., Ferrara A., Pallottini A., Carniani S., Gallerani S., 2020, *MNRAS*, 495, L22
- Vallini L., Ferrara A., Pallottini A., Carniani S., Gallerani S., 2021, *MNRAS*, 505, 5543
- Vanzella E. et al., 2017, *MNRAS*, 467, 4304
- Vanzella E. et al., 2019, *MNRAS*, 483, 3618
- van der Walt S., Colbert S. C., Varoquaux G., 2011, *Comput. Sci. Eng.*, 13, 22
- Van Rossum G., de Boer J., 1991, *CWI Q.*, 4, 283
- Van Rossum G., Drake F. L., 2009, *Python 3 Reference Manual*. CreateSpace, Scotts Valley, CA
- Virtanen P. et al., 2020, *Nat. Methods*, 17, 261
- Walter F. et al., 2018, *ApJ*, 869, L22
- Watson D., Christensen L., Knudsen K. K., Richard J., Gallazzi A., Michałowski M. J., 2015, *Nature*, 519, 327
- Weaver R., McCray R., Castor J., Shapiro P., Moore R., 1977, *ApJ*, 218, 377
- Webber W. R., 1998, *ApJ*, 506, 329
- Weingartner J. C., Draine B. T., 2001, *ApJ*, 563, 842
- Wilkins S. M., Feng Y., Di-Matteo T., Croft R., Stanway E. R., Bunker A., Waters D., Lovell C., 2016, *MNRAS*, 460, 3170
- Willott C. J., Carilli C. L., Wagg J., Wang R., 2015, *ApJ*, 807, 180
- Wise J. H., Abel T., Turk M. J., Norman M. L., Smith B. D., 2012, *MNRAS*, 427, 311
- Wiseman P., Schady P., Bolmer J., Krühler T., Yates R. M., Greiner J., Fynbo J. P. U., 2017, *A&A*, 599, A24
- Xu H., Wise J. H., Norman M. L., Ahn K., O’Shea B. W., 2016, *ApJ*, 833, 84
- Zanella A. et al., 2018, *MNRAS*, 481, 1976
- Zanella A., Pallottini A., Ferrara A., Gallerani S., Carniani S., Kohandel M., Behrens C., 2021, *MNRAS*, 500, 118

This paper has been typeset from a $\text{\TeX}/\text{\LaTeX}$ file prepared by the author.